

## A DETAILED INVESTIGATION OF PROJECTION EFFECTS RELEVANT TO THE STUDY OF POWERFUL CLASSICAL DOUBLE RADIO SOURCES

LIN WAN AND RUTH A. DALY<sup>1</sup>

Department of Physics, Princeton University, Princeton, NJ 08544

Received 1997 August 6; accepted 1998 January 12

### ABSTRACT

A detailed investigation of projection effects involved in the study of classical double sources is presented here. Theoretical calculations of the way projection effects enter empirically determined parameters are studied. It is shown that some parameters, such as the lobe width, are rather insensitive to the projection angle, while other parameters, such as the ambient gas density, are more sensitive.

The deviation of the observed value from the true value of any given parameter is usually not significant when the projection angle is greater than about 60° and is significant only at very small projection angle, at which the symmetry axis of the source is pointing close to the line of sight to the observer.

Applications of the theoretical model to a sample of classical double radio sources yield the following principal results:

1. A comparison between the radio-loud quasars and the radio galaxies in the sample suggests that their average projection angles are very similar. The average projection angle of the radio-loud quasars in the sample is greater than 35°–40° at the 3  $\sigma$  level, assuming that the average projection angle of radio galaxies is 70° or above.

2. On average, the low-redshift radio-loud quasars in the sample have much lower lobe surface brightness and lower nonthermal pressure than the low-redshift radio galaxies, a result which cannot be explained by projection effects. This is consistent with the fact that the radio-loud quasars appear to be “fatter” than the radio galaxies, as previously noted by Leahy, Muxlow, & Stephens.

3. The study of departures of the magnetic field strength from that estimated using the minimum-energy conditions suggests that the projection angle of Cygnus A is greater than about 40° (at 3  $\sigma$ ) to 55° (at 2  $\sigma$ ), in agreement with the independent results of Sorathia et al. These departures also indicate that the projection angles of most of the sources in the sample, including galaxies and quasars, are likely to be greater than about 30° (at 3  $\sigma$ ) to 40° (at 2  $\sigma$ ). This result does not depend on any assumptions about the average projection angle of radio galaxies and is consistent with result 1 stated above.

Thus, it is very unlikely that projection significantly affects key parameters, such as the ambient gas temperature and density, for the sources studied here.

*Subject headings:* galaxies: active — galaxies: magnetic fields — methods: analytical — quasars: general — radio continuum: galaxies

### 1. INTRODUCTION

Projection effects have always been an important issue in astrophysical studies. The not-directly observable projection angle of an astrophysical object can cause the observed values of parameters of the object to deviate from their intrinsic values. The same object may even be classified as different objects when projected at different angles toward the observer, as is believed to be the case in the orientation-unified model for powerful radio sources (see, e.g., Barthel 1989; Antonucci 1993; Gopal-Krishna, Kulkarni, & Mangalam 1994), in which a radio-loud quasar appears as a radio galaxy when its radio axis lies outside a certain angle with respect to the observer’s line of sight. Thus, any interpretation of observational results should consider possible projection effects.

This paper addresses the issue of projection effects in the study of powerful FR II radio sources (Fanaroff & Riley 1974). In particular, a sample of powerful FR II radio sources have been carefully studied by Daly and collaborators. Results on important parameters of these sources, such as the ambient gas density and temperature, the luminosity in kinetic energy of the jet, and the “characteristic”

size of the source, have been presented (Daly 1994, 1995; Wellman & Daly 1996a, 1996b; Wan & Daly 1998; Guerra & Daly 1998; Wellman, Daly, & Wan 1997a, 1997b; hereafter WDW97a, WDW97b, respectively). This paper investigates how projection effects enter into the determination of these parameters. In addition, the radio galaxies and the radio-loud quasars in the sample will be compared with each other to determine whether the observed differences between them can be explained by projection effects.

The powerful FR II sources used in this study are compiled using the samples of Leahy, Muxlow, & Stephens (1989; hereafter LMS89), and Liu, Pooley, & Riley (1992; hereafter LPR92). LMS89 selected powerful 3CR sources with large angular sizes (angular size greater than 20”), while LPR92 chose powerful 3CR sources of small angular extent (angular size less than 45”). A few sources from the LMS89 and LPR92 samples are not included in the final sample either because they fall below the power cut of  $P_{178} > 3 \times 10^{26} \text{ h}^{-2} \text{ W Hz}^{-1} \text{ sr}^{-1}$ , where  $P_{178}$  is the radio power at 178 MHz, or because their lobes have peculiar morphology. Another few sources, most of which are the smallest sources from the LPR92 sample, are excluded because the observed portions of their radio bridges are not extended enough. The final sample contains 27 radio lobes from 14 FR II radio galaxies, and 14 lobes from eight FR II

<sup>1</sup> National Young Investigator.

radio-loud quasars, with redshifts between 0 and 2 and core-hotspot separations ranging from 25 to 250  $h^{-1}$  kpc. More detailed descriptions of the sample have been given elsewhere (see WDW97a; WDW97b).

The rest of this paper is structured as follows. A theoretical model of the classical double sources studied here is presented in § 2. The way that projection effects alter the empirically determined values of various parameters of an FR II radio source is discussed in § 3. Detailed results for the sample, such as constraints on the projection angles of the sources in the sample and the differences between radio galaxies and radio-loud quasars and their implications, are presented in § 4. A summary of the paper and further discussions are presented in § 5.

Hubble's constant  $H_0 = 100 h \text{ km s}^{-1} \text{ Mpc}^{-1}$  and the de/acceleration parameter  $q_0 = 0$  are used to estimate all the parameters in this study.

## 2. SOURCE MODEL

A schematic of an FR II radio source with a projection angle  $\theta$  is shown in Figure 1. Only the cross section of the source in the plane defined by the line of sight, and the radio axis is shown in the figure. The direction along the radio axis is defined as the  $x$ -direction, and the direction perpendicular to the radio axis in this plane is the  $y$ -direction. The direction perpendicular to this  $x - y$  plane is defined as the  $z$ -direction and is not shown in the figure. Cylindrical symmetry about the radio axis is assumed for the source. Thus at a given distance  $x$  from the hotspot, the half-width of the source, i.e., the radius of the cross section, is given by

$$a(x) = \sqrt{y^2 + z^2}. \quad (1)$$

The study carried out by WDW97a showed that the bridges of FR II radio sources undergo lateral expansion before they reach pressure equilibrium with the ambient

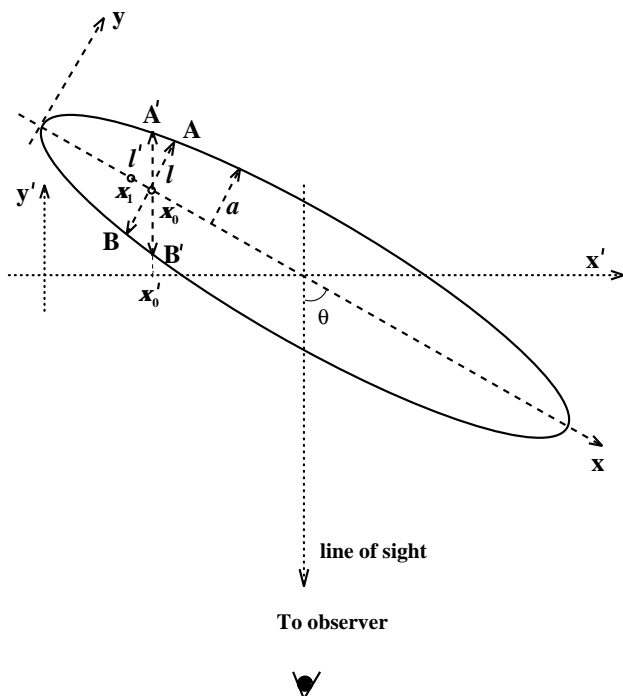


FIG. 1.—Diagram of an FR II source with a projection angle  $\theta$ . Shown in the figure is the cross section of the source in the plane defined by the line of sight and the radio axis, which is defined as the  $x$ -direction. The projection of  $x$  in the observer's frame is the  $x'$ -direction.

gas. This is illustrated in Figure 1. The observed form of the lateral expansion is approximately  $a(x) \propto x^{1/2}$ , which is consistent with the model predictions given by Daly (1990) and by Begelman & Cioffi (1989). Thus, in this study of projection effects, the shape of the radio source is taken to be

$$a(x) = k_L x^{1/2}, \quad (2)$$

where  $k_L$  is a constant that is different for each source.

Most of the sources studied here have  $k_L$  ranging between 1 and 4 (WDW97a). More specifically, about 25% of the sources have  $k_L$  between 1.25 and 1.75,  $\sim 35\%$  have  $k_L$  between 1.75 and 2.25,  $\sim 25\%$  have  $k_L$  between 2.25 and 2.75,  $\sim 10\%$  have  $k_L$  between 2.75 and 3.25, and  $\sim 10\%$  have  $k_L$  between 3.25 and 4.5 (see Table 1 in WDW97a for a listing of  $k_L$ ).

As the radio-emitting plasma in the radio bridge expands, it cools and its volume emissivity decreases. Assuming that the lateral expansion is adiabatic and that the reacceleration of relativistic electrons and backflow of relativistic plasma are negligible within the radio bridge, all of which are suggested by the data (see WDW97a), the relation between the volume emissivity  $\epsilon$  and the amount of expansion is

$$\epsilon(x) \propto a(x)^{(8/3\alpha - 10/3)}, \quad (3a)$$

where  $\alpha$  is the radio spectral index of the source, defined such that the flux density  $f_\nu \propto \nu^\alpha$ . An implicit assumption of this relation is that the volume emissivity is homogeneous in the cross section at a given distance  $x$  from the hotspot, i.e., the emissivity is a function of only the distance  $x$ . This expansion model works quite well for most of the sources in this sample (WDW97a) and is thus taken to be the underlying expansion model in this study. Substituting equation (2) into equation (3a), the emissivity can be expressed as

$$\epsilon(x) \propto x^{(4/3\alpha - 5/3)} \propto x^\gamma, \quad (3b)$$

where  $\gamma$  is defined as  $\gamma \equiv \frac{4}{3}\alpha - \frac{5}{3}$ . For  $\alpha = -0.7$ , which is a typical value for the sources studied here, the value of  $\gamma$  is  $-2.6$ ; this typical value of  $\gamma$  is used in the theoretical calculations throughout the paper.

Equations (3a) and (3b) hold as long as energy loss due to spectral aging is negligible, which is usually true at low radio frequency. At high radio frequency, the effect of spectral aging is usually not negligible and the emissivity should be modeled differently (see § 3.6.2). Except for the radio spectral index that is used in the spectral aging analysis, all other parameters discussed in this paper are estimated using low-frequency radio maps, for which equations (3a) and (3b) are good descriptions of the volume emissivity.

## 3. THEORY

The unknown projection angle of an FR II source affects the observed or "apparent" values of source parameters. The simplest example is the size of a source, with  $l_{\text{observed}} = l_{\text{true}} \sin \theta$ . The way projection affects the values of various parameters, given the source model described in § 2, is studied in § 3.1 through § 3.6. A summary of this section is presented in § 3.7.

All primed symbols in this section refer to observed or "apparent" values, whereas true physical values are denoted with unprimed symbols.

3.1. Length and Linear Size

It is obvious from Figure 1 that all measurements of length along the  $x$  direction are affected by a factor of  $\sin \theta$ , whereas length measurements along the  $z$ -direction, i.e., perpendicular to the radio axis and in the plane of the sky, remain unchanged. Among the affected length measurements are the distance from the hotspot ( $x$ ), the distance between two points along the radio bridge ( $\Delta D$ ), and the linear size of the source, represented by the core-hotspot separation of the source ( $r$ ). The observed values for  $x$ ,  $\Delta D$ , and  $r$  are

$$\begin{cases} x' = x \sin \theta \\ \Delta D' = \Delta D \sin \theta \\ r' = r \sin \theta . \end{cases} \quad (4)$$

A point that is at an apparent distance  $x'_0$  away from the hotspot in the observer's frame is actually at a real distance  $x_0$  away from the hotspot in the source frame, where  $x'_0 = x_0 \sin \theta$ . Note that although  $x_0$  in the source frame and  $x'_0$  in the observer's frame have different numerical values, they actually refer to the same point along the radio axis, whereas a point at a true distance  $x_1$  that has the same value as  $x'_0$ , that is,  $x_1 = x'_0$ , is actually a different point along the radio axis (see Fig. 1).

3.2. Surface Brightness

The surface brightness of a radio sources is given by  $S \propto \int \epsilon dl$ , where the integration is along the line of sight. When the line of sight is perpendicular to the radio axis, this gives the real surface brightness of the source  $S_r$ . In this case, the emissivity  $\epsilon$  is a constant along the line of sight. Thus the real surface brightness at  $x$  can be expressed as

$$S_r(x, z) \propto \epsilon(x)l(x, z), \quad (5)$$

where  $z$  is the height from the radio axis and  $l(x, z)$  is the line of sight depth at that point (the segment between point  $A$  and point  $B$  in Fig. 1), which is given by

$$l(x, z) = 2y(x, z) = 2\sqrt{a(x)^2 - z^2}. \quad (6)$$

Here equation (1) is used to get the expression for  $y(x, z)$ . Combining these two equations, it is easy to show that

$$S_r(x, z) = S_r(x, 0)\sqrt{1 - \left(\frac{z}{a(x)}\right)^2}, \quad (7a)$$

where  $S_r(x, 0)$  is the surface brightness along the radio axis at  $x$  and is given by

$$S_r(x, 0) \propto 2a(x)\epsilon(x). \quad (7b)$$

When the source is projected at an angle  $\theta$  rather than seen edge on, two factors affect the observed surface brightness  $S'$ . First, the observed surface brightness at an apparent distance  $x'_0$  away from the hotspot is actually the surface brightness at a real distance  $x_0$  from the hotspot, where  $x'_0 = x_0 \sin \theta$  (eq. [4]). Second, the line of sight now crosses regions at different distance  $x$  from the hotspot and its length also changes.

The observed surface brightness is now

$$S'(x'_0, z) \propto \int_{A'}^{B'} \epsilon(x)dl, \quad (8a)$$

where  $A'$  and  $B'$  are the points of intersection of the line of sight and the surface of the source. The line element

$dl = dx/\cos \theta$ . Thus  $S'(x'_0, z)$  can also be written as

$$S'(x'_0, z) \propto \int_{x_{A'}}^{x_{B'}} \epsilon(x) \frac{dx}{\cos \theta}, \quad (8b)$$

where  $x_{A'}$  and  $x_{B'}$  are the  $x$  coordinates of  $A'$  and  $B'$ . The values of  $x_{A'}$  and  $x_{B'}$  can be derived as follows. The boundary of the cross section of the source at any given height  $z$  away from the radio axis is given by the curve

$$y = \sqrt{a(x)^2 - z^2} = \sqrt{k_L^2 x^2 - z^2}, \quad (9a)$$

which can be easily derived using equation (1) and equation (2). The line of sight passing a given point  $x_0$  is given by

$$y = C(x - x_0), \quad (9b)$$

where  $C$  is the slope of the line of sight, and  $C \equiv \tan \theta$ . These two curves intersect at

$$\begin{cases} x_{A'} = x_0 + \frac{k_L^2}{2C^2} - \frac{1}{C} \sqrt{k_L^2 x_0 + \frac{k_L^4}{4C^2} - z^2} \\ x_{B'} = x_0 + \frac{k_L^2}{2C^2} + \frac{1}{C} \sqrt{k_L^2 x_0 + \frac{k_L^4}{4C^2} - z^2} . \end{cases} \quad (10)$$

Recall from equation (3b) that  $\epsilon(x) \propto x^\gamma$ , so we can write  $\epsilon(x)$  as  $\epsilon(x) = \epsilon(x_0)(x/x_0)^\gamma$ . Thus

$$S'(x'_0, z) \propto \frac{1}{\cos \theta} \frac{\epsilon(x_0)}{x_0^\gamma} \int_{x_{A'}}^{x_{B'}} x^\gamma dx \quad (11a)$$

Equations (11a) and (10) together give the complete expression for the observed surface brightness at a projected distance  $x'_0$  in terms of the real distance  $x_0$ , which equals  $x'_0/\sin \theta$ , and the emissivity at  $x_0$ . However, often what we want to compare is the observed surface brightness at a projected distance  $x'_0$  with the real surface brightness at a true distance  $x_1$  that has the same value as  $x'_0$ . A good example is a comparison between the observed surface brightness at a projected distance of  $10 h^{-1}$  kpc with the real surface brightness at a true distance of  $10 h^{-1}$  kpc. That is, we want to compare  $S'(x'_0, z)$  with  $S_r(x_1, z)$ , where  $x_1$  and  $x'_0$  have the same value, i.e.,  $x_1 = x'_0$ . Thus, it is more convenient to express  $S'(x'_0, z)$  in terms of  $x_1$  and  $\epsilon(x_1)$ . Since  $\epsilon(x_0)/x_0^\gamma = \epsilon(x_1)/x_1^\gamma$ , as can be inferred from equation (3b), equation (11a) can be rewritten as

$$S'(x'_0, z) \propto \frac{1}{\cos \theta} \frac{\epsilon(x_1)}{x_1^\gamma} \int_{x_{A'}}^{x_{B'}} x^\gamma dx, \quad (11b)$$

where  $x_{A'}$  and  $x_{B'}$  are those given in equation (10), with  $x_0 = x'_0/\sin \theta$  and  $x_1 = x'_0$ .

Figure 2 illustrates how the observed surface brightness in a slice perpendicular to the radio axis deviates from the real value because of projection. It can be seen that both the peak value and the shape of the surface brightness profile change with projection angle. For a large value of  $\theta$ ,  $\theta = 60^\circ$  for example, the observed profile and the real one are very close, while for small  $\theta$ , they can be quite different. This means that a careful study of the surface brightness profile of an FR II source can serve as a diagnosis of its projection angle, provided the resolution of its radio map is high enough to allow such a study. Note that anisotropic magnetic field in the FR II source can also cause the surface brightness profile to deviate from that in a homogeneous emissivity model (eq. [7a]; see Laing 1980, 1981). Such an

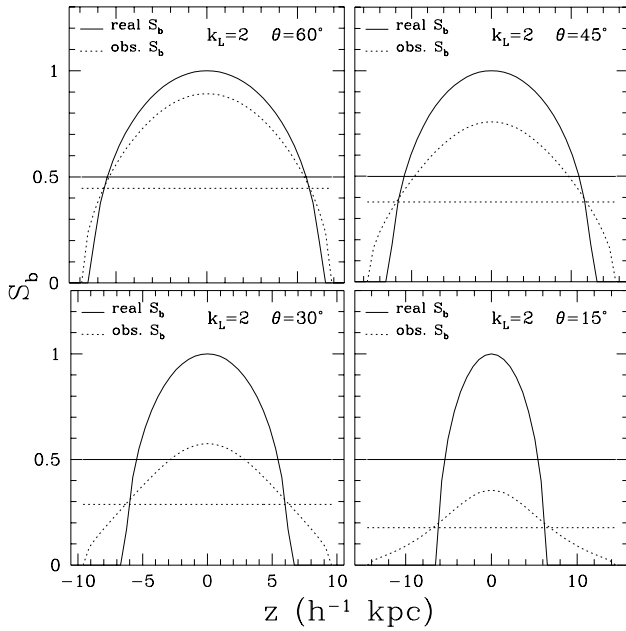


FIG. 2.—Surface brightness profile at  $10 h^{-1}$  kpc away from the hotspot vs. the height from the radio axis for an FR II source at different projection angles. The solid curve is the real surface brightness at a true distance of  $10 h^{-1}$  kpc from the hotspot. The dotted curve is the observed surface brightness at a projected distance of  $10 h^{-1}$  kpc from the hotspot. The lines correspond to the half-maximum of the real and observed surface brightnesses. The surface brightness is normalized so that the peak real surface brightness has a value of 1. The source here has  $k_L = 2$  and  $\alpha = -0.7$ , which are typical values for the sources studied here.

anisotropic magnetic field would also cause the source to have high polarization. The radio bridges of powerful extended sources, which are the regions relevant to this study, usually have low or moderate degrees of polarization (see, e.g., Garrington, Conway, & Leahy 1991; Fernini et al. 1993). Polarization data are available for several sources in this sample. The percentage polarization in their radio bridges are typically below 10%. Thus it appears that the effect of anisotropic emission is unlikely to be significant here, though projection effects may be significant.

One consequence of the change in the shape of the surface brightness profile is that its full width at half maximum (FWHM) also changes, which will in turn affect the observed value of the width of source. This will be discussed in § 3.3.

The peak value of the surface brightness, or the surface brightness along the radio axis (referred to as  $S_0$  hereafter), is used in the calculation of many other parameters. Thus it is important to study how projection affects this parameter. Figure 3 is a plot of the ratio of the observed surface brightness along the radio axis  $S'_0(x'_0)$  to the real value  $S_0(x_1)$ , where  $x_1 = x'_0$ , as a function of the distance from the hotspot. For simplicity, the ratio  $S'_0(x'_0)/S_0(x_1)$  will be referred to as  $S'_0/S_0$  hereafter. This notation will be used throughout the paper. For any parameter  $Y$  studied here that is a function of the distance from the hotspot, such as the surface brightness  $S$ , the half-width of the source  $a$ , and the magnetic field strength  $B$ , the ratio  $Y'/Y$  is defined as the ratio of the observed value of  $Y$  at a projected distance  $x'_0$  to the intrinsic value of  $Y$  at a true distance  $x_1$ , where  $x_1$  and  $x'_0$  have the same value, i.e.,  $Y'/Y \equiv Y'(x'_0)/Y(x_1)$  and  $x_1 = x'_0$ .

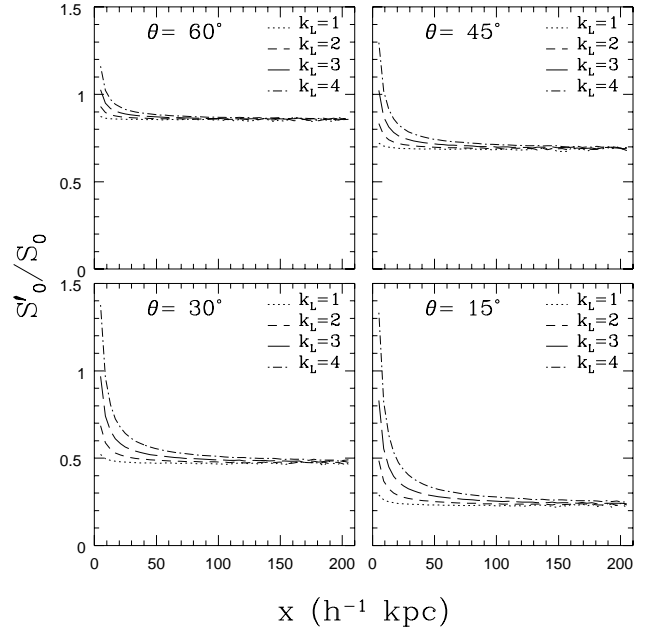


FIG. 3.—Ratio of the observed value of the surface brightness along the radio axis to the true value as a function of the distance from the radio axis for an FR II source with different projection angles.

It can be seen that the ratio  $S'_0/S_0$  varies with projection angle and is closer to 1 for larger  $\theta$ , as expected. At large distances from the hotspot, the ratio is almost a constant whose value is approximately  $(\sin \theta)^{1.1}$ . This is to be expected from equation (11b). The ratio of the observed value to the real value is

$$\frac{S'(x'_0, 0)}{S_r(x_1, 0)} = \frac{(1/\cos \theta)[\epsilon(x_1/x'_1)] \int_{x_{A'}}^{x_{B'}} x' dx}{2a(x_1)\epsilon(x_1)} = \frac{1}{\cos \theta} \frac{1}{2k_L x_1^{\gamma+1/2}} \frac{1}{\gamma+1} [x_{B'}^{\gamma+1} - x_{A'}^{\gamma+1}], \quad (12)$$

where  $x_1 = x'_0$ . The values of  $x_{A'}$  and  $x_{B'}$  are given in equation (10). At large distances from the hotspot, where the condition  $x_0 C^2/k_L^2 \gg 1$  is satisfied,  $x_{A'}$  and  $x_{B'}$  can be approximated as

$$\begin{cases} x_{A'} \approx x_0 - \frac{1}{C} k_L x_0^{1/2} \\ x_{B'} \approx x_0 + \frac{1}{C} k_L x_0^{1/2}, \end{cases} \quad (13a)$$

where  $C \equiv \tan \theta$ . Using these approximate forms for  $x_{A'}$  and  $x_{B'}$ , it is easy to show that when  $x_0 C^2/k_L^2 \gg 1$ ,

$$x_{B'}^{\gamma+1} - x_{A'}^{\gamma+1} \approx 2 \left( \frac{\gamma+1}{C} \right) k_L x_0^{\gamma+1/2}. \quad (13b)$$

Combining equations (12) and (13b), we have

$$\frac{S'(x'_0, 0)}{S_r(x_1, 0)} \approx \frac{1}{\cos \theta} \frac{1}{C} \left( \frac{x_0}{x_1} \right)^{\gamma+1/2}. \quad (14a)$$

Since  $x_1 = x'_0$ ,  $x_0/x'_0 = 1/\sin \theta$ , and  $C \equiv \tan \theta$ , this becomes

$$\frac{S'(x'_0, 0)}{S_r(x_1, 0)} \approx (\sin \theta)^{-(\gamma+1.5)}. \quad (14b)$$

For the typical value  $\gamma = -2.6$ , which corresponds to  $\alpha = -0.7$ , the above relation gives

$$\frac{S'(x'_0, 0)}{S_0(x_1, 0)} \approx (\sin \theta)^{1.1} . \quad (14c)$$

For the sources studied here, this is usually a good approximation when  $x \gtrsim 50 h^{-1}$  kpc.

The ratio  $S'_0/S_0$  differs from the approximation given by equation (14c) at small distances from the hotspot. Figure 4 plots  $S'_0/S_0$  versus  $\theta$  at  $10 h^{-1}$  kpc from the hotspot. It can be seen that  $S'_0/S_0$  at  $10 h^{-1}$  kpc from the hotspot is usually different from  $(\sin \theta)^{1.1}$ , especially for large values of  $k_L$ . The observed surface brightness is usually within 20% of the true value when  $\theta > 50^\circ$ , but for a small projection angle  $\theta$ , the observed value can be quite different from the real one, especially for sources with small  $k_L$ . For an ensemble of sources, the ratio of the average observed surface brightness ( $\langle S'_0 \rangle$ ) to the average real surface brightness ( $\langle S_0 \rangle$ ) can be estimated using the average value of  $S'_0/S_0$  because  $S'_0/S_0$  is not correlated with  $S_0$  or  $S'_0$ . This can be expressed as  $\langle S'_0 \rangle / \langle S_0 \rangle \cong \langle S'_0/S_0 \rangle$ . The value of  $\langle S'_0/S_0 \rangle$  for a sample of sources with different  $k_L$  can be estimated once the distribution of  $k_L$  is known for the population. The  $k_L$  distribution for the sample studied here is described in § 2, and the corresponding  $\langle S'_0/S_0 \rangle$  at  $10 h^{-1}$  kpc from the hotspot is plotted as the solid line in Figure 4.

### 3.3. Source Width

The observed width of a radio source is compared with the real width in this section. Of particular interest is the lobe width of a source, measured at  $10 h^{-1}$  kpc behind the hotspot, which is used to estimate many of the other physical parameters. It will be shown that for most of the sources studied here, the observed lobe width is not significantly

affected by projection and is rather close to the real value for almost any projection angle.

The half-width of a radio source a distance  $x$  away from the hotspot is estimated using the FWHM of the surface brightness profile at that point. The real surface brightness profile is that described by equation (7a). For such a surface brightness profile, it's easy to show that  $\text{FWHM}(x) = (3)^{1/2} a(x)$ , or  $a(x) = \text{FWHM}(x)/(3)^{1/2}$ . The observed half-width is estimated under the assumption that the observed surface brightness profile is the real one so that the above relation between  $a$  and the FWHM holds. Thus the formula used to calculate  $a'(x')$  is

$$a'(x') = \frac{\text{FWHM}'(x')}{\sqrt{3}} . \quad (15)$$

As mentioned in § 3.2, projection affects the shape of the observed surface brightness profile, and hence its FWHM as well (see Fig. 2). As a result, the observed half-width  $a'(x'_0)$  at a projected distance  $x'_0$  from the hotspot, estimated using equation (15), also differs from the real half-width  $a(x_1)$  at a real distance  $x_1$ , which is taken to have the same value as  $x'_0$ . Figure 5 illustrates how projection affects the observed width  $a'$ . The ratio  $a'/a$ , defined as  $a'(x'_0)/a(x_1)$ , is plotted versus the distance from the hotspot for four different values of  $\theta$ .

For a given  $\theta$ , the value of  $a'/a$  approaches a constant at large distances from the hotspot. This constant is  $(\sin \theta)^{-1/2}$ . A simple derivation of this is as follows. The observed surface brightness profile, given by equation (11b), has the following form:

$$S'(x'_0, z) = f \times [x_B^{\gamma+1} - x_A^{\gamma+1}] , \quad (16)$$

where  $f$  is a function of  $x$ ,  $\theta$ ,  $k_L$ , and  $\gamma$ . Since  $f$  does not depend on  $z$ , the  $z$ -dependence of  $S'$  comes entirely from the term containing  $x_A$  and  $x_B$ . It can be shown from equation (10) that at large distances, where  $x_0 C^2/k_L^2 \gg 1$ ,  $x_A$  and  $x_B$

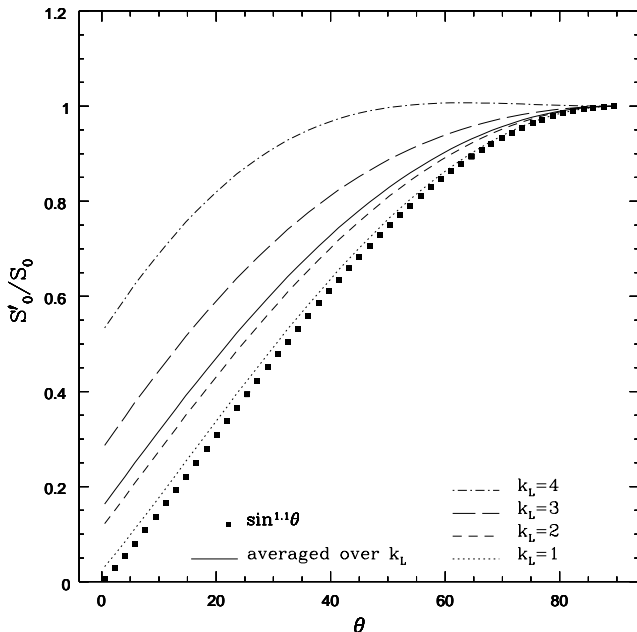


FIG. 4.—Ratio of the observed value of the lobe surface brightness, measured at  $10 h^{-1}$  kpc away from the hotspot, to the true value as a function of the projection angle. The solid curve is the average ratio expected for a sample of sources with the  $k_L$  distribution seen in our sample.

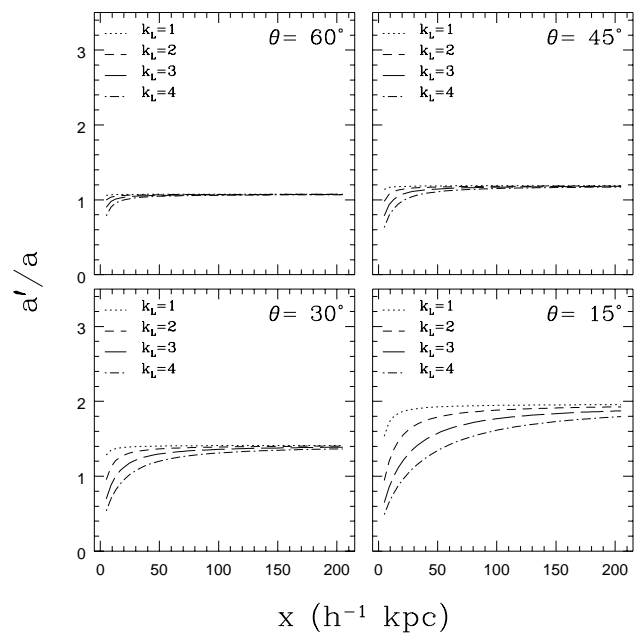


FIG. 5.—Ratio of the observed value of the half-width of the radio bridge to the true value as a function of the distance from the radio hotspot for an FR II source with different projection angles.

can be approximated as

$$\begin{cases} x_{A'} \approx x_0 - \frac{1}{C} \sqrt{k_L^2 x_0 - z^2} \\ x_{B'} \approx x_0 + \frac{1}{C} \sqrt{k_L^2 x_0 - z^2} \end{cases} \quad (17a)$$

This leads to

$$x_{B'}^{\gamma+1} - x_{A'}^{\gamma+1} \approx 2 \left( \frac{\gamma+1}{C} \right) x_0^{\gamma+1} \sqrt{\frac{k_L^2}{x_0} - \left( \frac{z}{x_0} \right)^2} \quad (17b)$$

Thus the observed surface brightness profile has the  $z$ -dependence

$$S'(x'_0, z) \propto \sqrt{1 - \left( \frac{z^2}{k_L^2 x_0} \right)} \propto \sqrt{1 - \left( \frac{z}{a(x_0)} \right)^2} \quad (18)$$

Comparing this with the real surface brightness profile (eq. [7a]), it's easy to see that at large distance, the shape of the observed surface brightness profile approaches the shape of the real surface brightness profile. It is easy to show that the FWHM of the observed surface brightness profile is  $\text{FWHM}' = (3)^{1/2} a(x_0) = (3)^{1/2} k_L x_0^{1/2}$ , which means that the observed half-width of the source is

$$a'(x'_0) = \frac{\text{FWHM}'(x'_0)}{\sqrt{3}} = a(x_0) \quad (19)$$

Thus we have

$$\frac{a'(x'_0)}{a(x_1)} = \frac{a(x_0)}{a(x_1)} = \frac{k_L x_0^{-1/2}}{k_L x_1^{-1/2}} = (\sin \theta)^{-1/2} \quad (20)$$

where the relations  $x_1 = x'_0$  and  $x'_0 = x_0 \sin \theta$  are used in the last step. Equation (20) is usually a good approximation for the sources studied here for  $x \gtrsim 50 h^{-1}$  kpc.

At smaller distances, the difference between  $a'$  and  $a$  is usually smaller than that given by equation (20). The lobe half-width of an FR II source, defined as  $a_L$ , is the half-width of the source at a true distance of  $10 h^{-1}$  kpc behind the hotspot. The observed lobe half-width  $a'_L$  is estimated at a projected distance of  $10 h^{-1}$  kpc behind the hotspot. Figure 6 plots the ratio  $a'_L/a_L$  versus  $\theta$ . The form of  $a'/a$  at large distances (i.e.,  $\sin^{-1/2} \theta$ ) is also plotted for comparison. For  $k_L = 2, 3$ , and  $4$ , which are the values of  $k_L$  for most of the sources studied here, the observed lobe half-width  $a'_L$  is rather close to the real value for almost any projection angle  $\theta$ . This means that the lobe half-widths estimated for the sources studied here are probably not significantly affected by projection.

### 3.4. Shape of the Source

The amount of projection effects on the observed width of an FR II source is a function of the distance from the hotspot (see Fig. 5). This causes the apparent shape of the source to deviate from the real shape (i.e., the observed width as a function of distance is different from the real shape  $a(x) = k_L x^{1/2}$ ). Figure 7 is a log-log plot of the half-width of a source with a  $k_L$  of 2 versus the distance from the hotspot. The real width  $a$  is a line with a slope of 0.5 and an intercept of  $\log 2$  in the figure. The observed width  $a'$  is represented by the dotted curve in the figure. It can be seen that the difference between  $a'$  and  $a$  increases with the distance from the hotspot at first. Then, at large distances, the

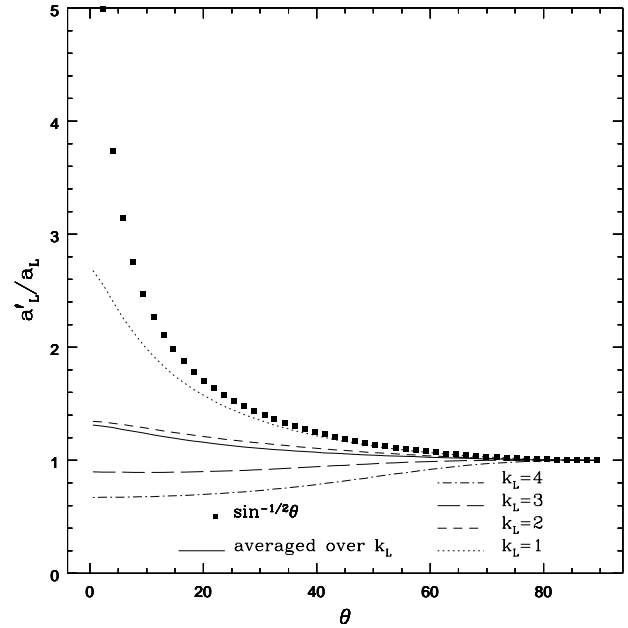


FIG. 6.—Ratio of the observed value of the lobe half-width, measured at  $10 h^{-1}$  kpc away from the hotspot, to the true value as a function of the projection angle. The solid curve is the average ratio expected for an ensemble of sources with the same  $k_L$  distribution as our sample.

curve representing the observed width becomes almost parallel to the line representing the real width, which is consistent with the fact that  $a'/a$  approaches a constant ( $\sin^{-1/2} \theta$ ) at large distances (§ 3.3).

One consequence of the above behavior of  $a'$  is that the observed value of  $k_L$ , estimated by fitting a line with a slope of 0.5 to the observed width  $a'(x')$  and finding the intercept, is closer to the true value for smaller sources than for larger sources, since the difference between  $a'$  and  $a$  is smaller at smaller distances from the hotspot. For large sources, for

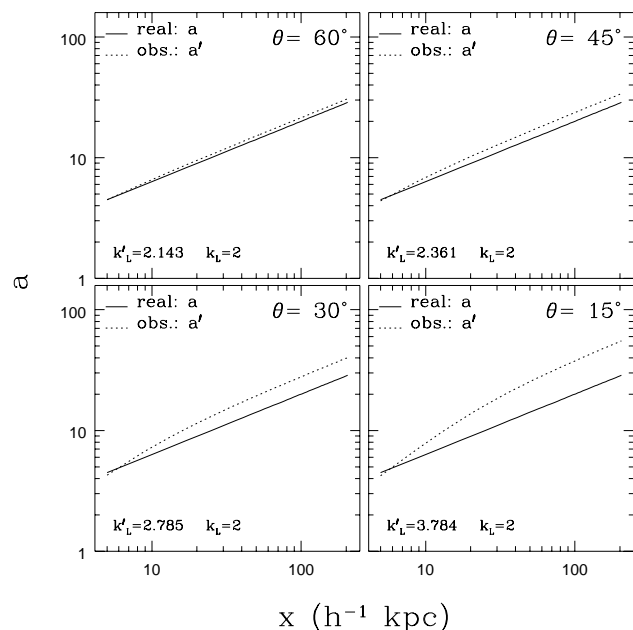


FIG. 7.—Observed and real half-width of the radio bridge as a function of the distance from the radio hotspot for an FR II source with different projection angles.

which there are numerous data points at large distances from the hotspot, the ratio  $k'_L/k_L$  will approach  $\sin^{-1/2} \theta$  as the ratio  $a'/a$  approaches  $\sin^{-1/2} \theta$ . Figure 8 is a plot of  $k'_L/k_L$  versus  $\theta$  for sources of different sizes. It indeed shows that  $k'_L/k_L$  is smaller for smaller sources and becomes closer to  $\sin^{-1/2} \theta$  for larger sources. However, this dependence of  $k'_L/k_L$  on source size is actually rather weak, and the difference occurs mostly at small projection angles. For  $\theta > 40^\circ$ , the observed value of  $k_L$  is usually within  $\sim 20\%$  of the real value, which is true for both small and large sources. It is shown in §§ 4.1 and 4.2 that the projection angles of the sources studied here are likely to be greater than  $35^\circ$ – $45^\circ$ . Thus, the observed values of  $k_L$  for the sources studied here are probably very close to their true values.

### 3.5. Surface Brightness as a Function of Lateral Expansion

Projection affects both the observed surface brightness and the observed width of the source. Thus the relation between the decrease in the surface brightness and the amount of lateral expansion will also be affected. Without projection, the real surface brightness along the radio axis is  $S_r(x, 0) \propto a(x)\epsilon(x)$  (eq. [7b]), and for adiabatic expansion,  $\epsilon(x) \propto a(x)^{8/3\alpha-10/3}$  (eq. [3a]). Hence, the relation between  $S_r(x, 0)$  and  $a(x)$  is the following power law:

$$S_r(x, 0) \propto a(x)\epsilon(x) \propto a(x)^{(8/3\alpha-7/3)}. \quad (21)$$

For a typical  $\alpha$  of  $-0.7$ , this gives  $S_r(x, 0) \propto a(x)^{-4.2}$ . Note that the power law relation in equation (21) is independent of the shape of the source  $a(x)$ . As long as the expansion is adiabatic, the above relation should always hold. WDW97a find that  $S_r(x, 0) \propto a(x)^{-(4-5)}$ , which is consistent with the prediction of equation (21) for sources with spectral indices ranging from  $-0.6$  to  $-0.9$ .

When an FR II source is projected at an angle  $\theta$ , the relation between the observed surface brightness along the radio axis ( $S'_0$ ) and the observed bridge half-width ( $a'$ ) will usually deviate from the power law given above. Figure 9 is

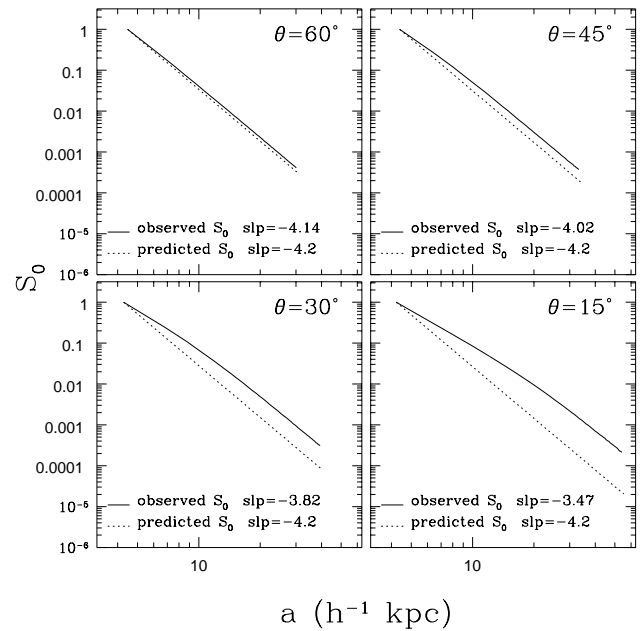


FIG. 9.—Surface brightness along the radio axis as a function of the amount of lateral expansion, represented by the half-width of the radio bridge, for an FR II source with different projection angles. The solid curve is the observed surface brightness. The dotted line is the surface brightness predicted by adiabatic expansion when there are no projection effects (eq. [21]). The source here has  $k_L = 2$  and  $\alpha = -0.7$ .

a log-log plot of  $S'_0$  versus  $a'$  for the case  $k_L = 2$ . The surface brightness predicted by equation (21) for the observed amount of lateral expansion when there is no projection effect is a line with a slope of  $-4.2$ , which corresponds to  $\alpha = -0.7$ . It can be seen that for small projection angles and large amounts of lateral expansion, the observed surface brightness can sometimes be quite different from the “predicted” value. As a result, the difference between the observed surface brightness and the predicted value can be used as a diagnosis of the projection angle, provided that the expansion is adiabatic and that complicating factors such as back flow and secondary hotspots in the radio bridge are negligible.

Projection effects on the observed surface brightness are also reflected in the overall slope of the observed curve in Figure 9. The best-fit slope of the observed curve, defined as  $n'$ , differs from the predicted slope of  $-4.2$ , and the difference increases with decreasing projection angle. Thus the observed slope  $n'$  can also be used as a diagnosis of the projection angle. There is a very weak dependence of  $n'$  on the size of the source because the slope of the observed curve is steeper for large  $a$ , which corresponds to large distances from the hotspot. This dependence can generally be ignored because of its weakness. For sources with sizes ranging from  $25 h^{-1}$  kpc to about  $200 h^{-1}$  kpc, the change in  $n'$  is usually less than 15%. Figure 10 is a plot of  $n'$  versus  $\theta$  for different values of  $k_L$ . The figure clearly illustrates how projection causes the observed slope  $n'$  to differ from the expected slope, especially for large  $k_L$  and small  $\theta$ .

### 3.6. Some Other Parameters

Most parameters studied by Daly (1994, 1995), WDW97a, WDW97b, Wan & Daly (1998), and Guerra & Daly (1998) are estimated using the observed surface brightness and the observed width of the source. Thus they are

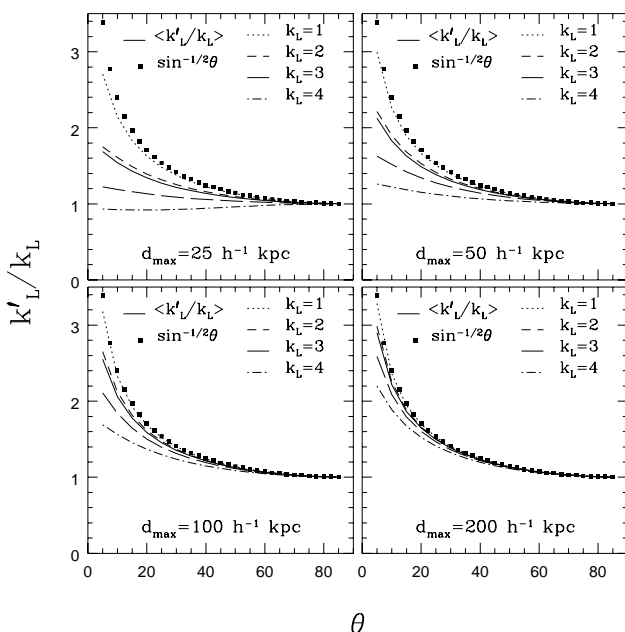


FIG. 8.—Ratio of the observed value of  $k_L$  to the true value as a function of the projection angle for sources whose linear sizes are 25, 50, 100, and  $200 h^{-1}$  kpc. The solid curve is the average ratio expected for a sample of sources with the  $k_L$  distribution seen in our sample.

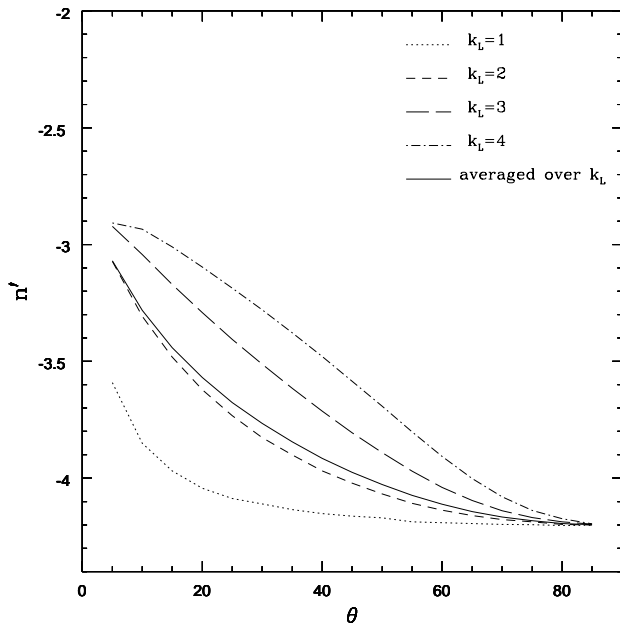


FIG. 10.—Best-fit slope for the observed curve in Fig. 9 vs. the projection angle. The solid curve is the average slope expected for a sample of sources with the  $k_L$  distribution seen in our sample. The expected slope when there is no projection effect is  $-4.2$ , which corresponds to  $\alpha = -0.7$ .

also affected by projection effects. In this section, we study the dependence of each of those parameters on the projection angle. The readers are referred to the papers listed above for more detailed description of how each parameter is estimated.

### 3.6.1. Magnetic Field Strength and Nonthermal Pressure

The minimum-energy magnetic field strength at a given point of an FR II source, defined as  $B_{\min}$ , can be estimated using the standard formula from Miley 1980 (see WDW97b; Wan & Daly 1998 for detailed description). The observed  $B'_{\min}$  has the following relation with the observed surface brightness along the radio axis ( $S'_0$ ) and the

observed source half-width ( $a'$ ):

$$B'_{\min} \propto \left( \frac{S'_0}{a'} \right)^{2/7}. \quad (22)$$

The nonthermal pressure at a given point can be estimated from  $B'_{\min}$  using

$$P'_{\text{nth}} \propto \left( \frac{4}{3} b^{-1.5} + b^2 \right) B'^2_{\min} \propto \left( \frac{S'_0}{a'} \right)^{4/7}, \quad (23)$$

where  $b$  is the ratio of the true magnetic field strength to the minimum-energy magnetic field strength ( $B = bB_{\min}$ ). WDW97b estimated  $b$  to be about 0.25, with a scatter from source to source of  $\sim 15\%$  (see WDW97b and references therein; Daly 1994, 1995; Wan & Daly 1998). This value of  $b$  does not seem to be significantly affected by projection effects, as is described in § 4.2.1, and is likely to be close to the true value of  $b$ . Wellman et al. (1997a, 1997b) also discussed the model with  $b = 1$ . Thus, both cases ( $b = 1$  and  $b = 1/4$ ) are considered in this paper.

The minimum-energy magnetic field strength in the radio lobe, defined as  $B_L$ , is the minimum-energy magnetic field strength at a true distance of  $10 h^{-1}$  kpc behind the hotspot toward the host source and is used to estimate the lobe nonthermal pressure  $P_L$ , using equation (23). The observed  $B'_L$  and  $P'_L$  are estimated at a projected distance of  $10 h^{-1}$  kpc behind the hotspot. Projection effects on the observed surface brightness and the observed width of the source have been discussed in §§ 3.2 and 3.3. In particular, Figures 4 and 6 show how  $S'_0/S_0$  and  $a'/a$  vary with  $\theta$  at  $10 h^{-1}$  kpc behind the hotspot. Knowing  $S'_0/S_0$  and  $a'/a$ , it is easy to calculate the ratio of the observed lobe pressure to the real lobe pressure, since  $P'/P = (S'_0/S_0)^{4/7} (a'/a)^{-4/7}$ . Figure 11a is a plot of  $P'_L/P_L$  versus  $\theta$ . At large distances from the hotspot,  $S'_0/S_0 \sim \sin^{1.1} \theta$  and  $a'/a \sim \sin^{-0.5} \theta$  (§§ 3.2 and 3.3), which means  $P'/P \sim \sin^{0.91} \theta$ . This asymptotic form of  $P'/P$  usually holds for  $x \gg 50 h^{-1}$  kpc for the sources studied here and is also plotted in the figure.

The average minimum-energy magnetic field strength in the radio bridge of an FR II source,  $B_b$ , is needed in order to

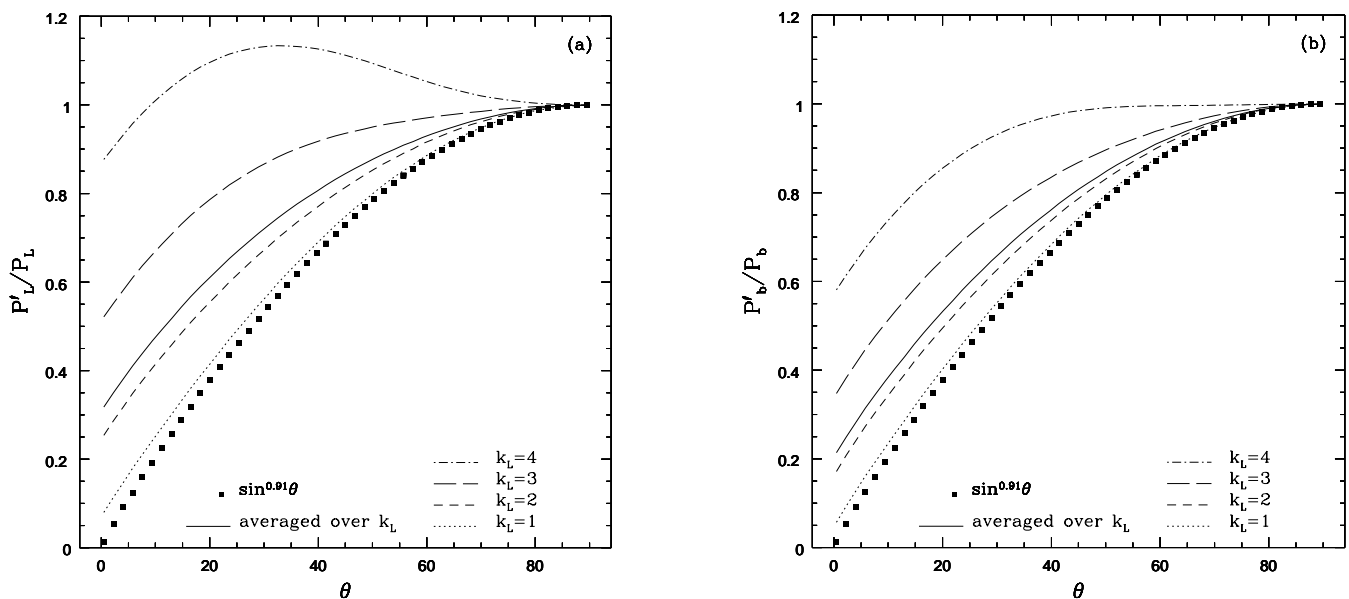


FIG. 11.—The ratio of the observed value of the nonthermal pressure in (a) the radio lobe and (b) the radio bridge to the true value as a function of the projection angle at  $d = 10 h^{-1}$  kpc. The solid curve is the average ratio expected for a sample of sources with the  $k_L$  distribution seen in our sample.

estimate the lobe propagation velocity (see § 3.6.3). A good estimate of  $B_b$  is  $(B_{10} B_{25})^{1/2}$ , where  $B_{10}$  and  $B_{25}$  are the minimum-energy magnetic field strengths at  $10 h^{-1}$  kpc and  $25 h^{-1}$  kpc behind the hotspot, respectively (for details, see WDW97a; WDW97b). The nonthermal pressure in the radio bridge, defined as  $P_b$ , can be estimated using  $B_b$  and equation (23). Figure 11b is a plot of  $P'_b/P_b$  versus  $\theta$ . The trend seen in the figure is similar to that in Figure 11a, except that  $P'_b/P_b$  is closer to the asymptotic form of  $P'/P$  at large distances,  $\sin^{0.91} \theta$ , than  $P'_L/P_L$  is.

Note that when  $\theta > 50^\circ$ , the difference between the observed nonthermal pressure and the real nonthermal pressure, either in the radio lobe or the radio bridge, is less than 20%. For smaller projection angle, the difference can be significant, especially for sources with small  $k_L$ , such as  $k_L = 1$  or 2.

### 3.6.2. The Radio Spectral Index

One key parameter used in the spectral aging analysis is the radio spectral index in the bridge of an FR II source. The study in this section will show that projection effects on the spectral index are unlikely to be significant for the sources studied here, while it may be important for other sources with very small linear sizes or very large  $k_L$ .

The radio spectral index in the bridge of an FR II source is usually a function of the distance from the hotspot. This spectral index variation is used in spectral aging analysis to estimate the break frequency  $\nu_T$  and the age of the relativistic electrons (see Jaffe & Perola 1973; Myers & Spangler 1985; Alexander & Leahy 1987; Alexander 1987; LMS89; Carilli et al. 1991; LPR92; WDW97b). When a source is projected at an angle  $\theta$ , the line of sight  $A'B'$  at a given point  $x_0$  passes through regions at different distances from the hotspot (see Fig. 1) that have different radio spectral indices. Thus the observed spectral index usually differs from the intrinsic value. The observed spectral index at  $x_0$  between two radio frequencies  $\nu_1$  and  $\nu_2$  is

$$\alpha'(x_0) = \frac{\log(S'_{\nu_1}/S'_{\nu_2})}{\log(\nu_1/\nu_2)}, \quad (24a)$$

where  $S'_{\nu_1}$  and  $S'_{\nu_2}$  are the observed surface brightnesses at  $\nu_1$  and  $\nu_2$  and are given by  $S'_{\nu_1} \propto \int_{A'}^{B'} \epsilon_{\nu_1}(x) dl$  and  $S'_{\nu_2} \propto \int_{A'}^{B'} \epsilon_{\nu_2}(x) dl$ . The low-frequency emissivity  $\epsilon_{\nu_1}(x)$  is usually not affected by aging and follows the adiabatic expansion law given in equations (3a) and (3b) (see § 2). The high-frequency emissivity  $\epsilon_{\nu_2}(x)$  can be estimated using  $\epsilon_{\nu_2} = \epsilon_{\nu_1}(\nu_2/\nu_1)^{\alpha(x)}$ , where the effect of aging has been taken into account in the variation of  $\alpha$  with  $x$  (here  $\alpha$  defined such that the flux density  $f_\nu \propto \nu^\alpha$ ). The function form of  $\alpha(x)$  can be quite complicated because of the combination of aging and expansion. Empirically, the spectral index in the bridge of an FR II source goes roughly as  $\alpha(x) \propto x$ . This empirical functional form is used in the calculation. The ratio  $S'_{\nu_1}/S'_{\nu_2}$  is given by

$$\frac{S'_{\nu_2}}{S'_{\nu_1}} = \frac{\int_{x_{A'}}^{x_{B'}} \epsilon_{\nu_1}(x) (\nu_2/\nu_1)^{\alpha(x)} dx}{\int_{x_{A'}}^{x_{B'}} \epsilon_{\nu_1}(x) dx}, \quad (24b)$$

where  $x_{A'}$  and  $x_{B'}$  are the  $x$  coordinates of  $A'$  and  $B'$ .

More than one third of the sources in our sample have a detected “break” in their bridge shapes, beyond which point the bridge no longer expands as  $a(x) \propto x^{1/2}$  but rather has a roughly constant width (see § 3.6.7 for details). For all these sources, the break frequency (or age) is measured in

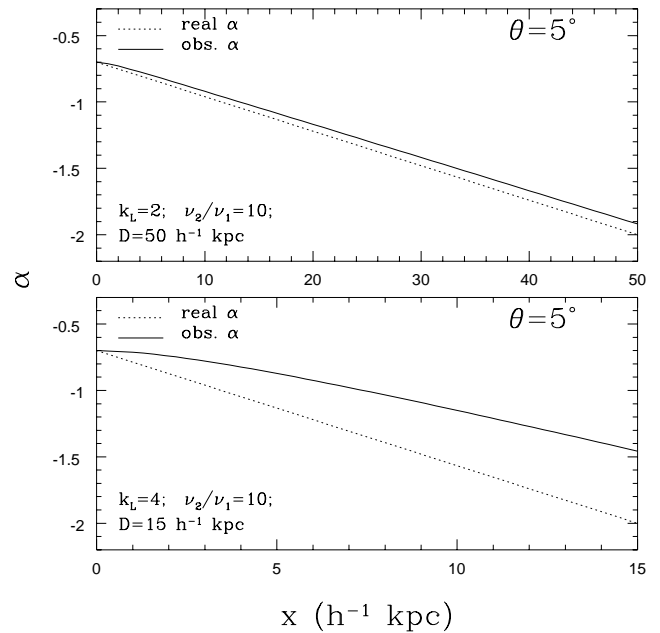


FIG. 12.—Observed and real radio spectral index vs. the projected distance from the hotspot for  $\theta = 5^\circ$ . The spectral index  $\alpha$  is defined such that the flux density  $f_\nu \propto \nu^\alpha$ .

the nonexpanding region of the source, where numerical calculations using equations (24a) and (24b) show that the difference between  $\alpha'(x_0)$  and  $\alpha(x_0)$  is no more than 5% for almost any projection angle. The typical difference between  $\alpha'$  and  $\alpha$  is only about 1% when the bridge is not expanding.

The rest of the sources studied here do not have detected “breaks” in their bridge shapes, and their bridges are still expanding at the point where the break frequency (or age) is measured. Figures 12 and 13 are illustrative plots of results from equations (24a) and (24b) when the bridge is expand-

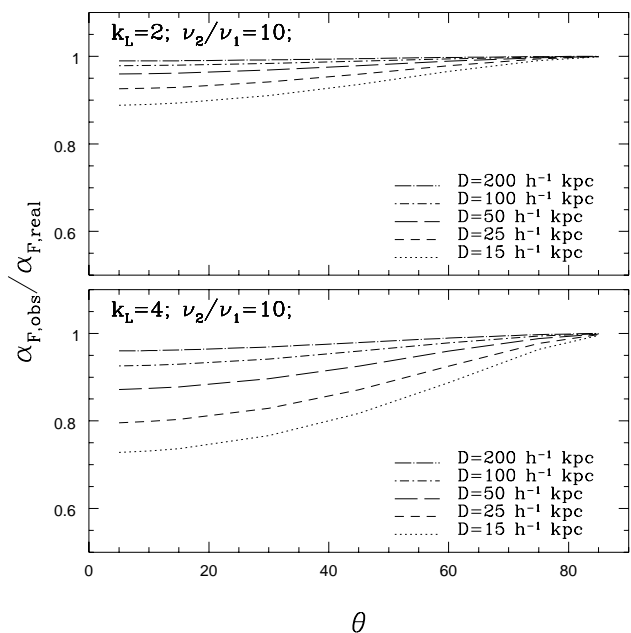


FIG. 13.—Ratio of the observed spectral index to the true value as a function of the projection angle. Here  $D$  is the projected distance between the hotspot and the point where the spectral index  $\alpha$  is measured.

ing. The upper panels in both figures correspond to typical sources in our sample, while the lower panels represent sources with large  $k_L$  and small sizes, which are not typical of the sources in our sample. It can be seen that while for sources with large  $k_L$  and small size, projection effects on  $\alpha$  can reach about 30%; for a typical source in our sample, the difference between  $\alpha'$  and  $\alpha$  is always less than about 10%. In fact, the variation in  $\alpha$  used in the calculation of Figure 13 is 1.3, which is much larger than the typical variation of  $\sim 0.7$  seen in the sources studied here. Thus, for the sources in our sample, the differences between the observed and real spectral indices are even less than that shown in Figure 13.

In summary, it appears that for the sources in our sample, whether there is a detected “break” in the bridge shape or not, the spectral index and the break frequency calculated using the spectral index are unlikely to suffer significant projection effects. Thus projection effects on these two parameters are neglected in the rest of the paper.

### 3.6.3. The Lobe Propagation Velocity

The propagation velocity of the lobe front ( $v_L$ ) is estimated by WDW97b using a synchrotron and inverse-Compton aging model. The observed value of  $v_L$  is given by

$$v'_L \propto \Delta D' v_T^{1/2} \left[ \frac{(bB'_b)^2 + B_{MB}^2}{(bB'_b)^{1/2}} \right], \quad (25)$$

where  $\Delta D'$  is the projected distance between two points along the radio axis,  $bB'_b$  is the observed average magnetic field strength in the radio bridge,  $B_{MB} = 0.318(1+z)^2 10^{-5}$  gauss is the equivalent magnetic field strength of the microwave background radiation, and  $v_T$  is the break frequency estimated using spectral aging analysis (see LMS89; LPR92; Myers, & Spangler 1985; WDW97b).

For  $b = 1$ , the value of  $bB'_b$  is usually much larger than  $B_{MB}$ . Thus  $v'_L$  is approximately

$$v'_L \propto \Delta D' (bB'_b)^{3/2}, \quad (26a)$$

where it has been assumed that the break frequency  $v_T$  does not suffer from projection effects, as was shown in § 3.6.2. Knowing how  $\Delta D'$  and  $B'$  are affected by projection

(eqs. [4] and [22]), it's easy to calculate how  $v'_L$  depends on the projection angle. Figure 14a is a plot of  $v'_L/v_L$  versus  $\theta$  for the case of  $b = 1$ . For  $\theta > 60^\circ$ , the observed value is within 20% of the true value, but for smaller  $\theta$ , the observed value of  $v_L$  can be quite different from the real value.

For  $b = 1/4$ , the value of  $bB'_b$  is usually comparable to that of  $B_{MB}$ . Thus  $v'_L$  is approximately

$$v'_L \propto \Delta D' (bB'_b)^{-1/2}. \quad (26b)$$

Figure 14b plots  $v'_L/v_L$  versus  $\theta$  for this case. It appears that for  $b = 1/4$ , the observed value of  $v_L$  is still rather sensitive to the projection angle, though not as strongly as for the  $b = 1$  case. For  $\theta > 50^\circ$ , the observed value is within 20% of the true value, whereas for smaller  $\theta$ , the observed value of  $v_L$  can be quite different from the real value.

### 3.6.4. Ambient Gas Density

The ambient gas density ( $n_a$ ) in the vicinity of an FR II source can be estimated using ram-pressure confinement of the radio lobe. The expression for the observed value of  $n_a$  is

$$n'_a \propto \frac{P'_L}{v_L'^2}. \quad (27)$$

The ratio  $n'_a/n_a$  can be estimated using the results on  $P'_L$  and  $v'_L$  obtained above. Figures 15a and 15b are log-linear plots of  $n'_a/n_a$  versus  $\theta$  for  $b = 1$  and  $b = 1/4$ , respectively. It can be seen from the figures that the observed value of  $n_a$  is rather sensitive to the projection angle, especially for the  $b = 1$  case, and can be quite different from the true value at small projection angles. For  $\theta > 60^\circ$ , the observed value is usually within 40% of the true value, whereas for smaller  $\theta$ , the difference between  $n'_a$  and  $n_a$  increases rapidly as  $\theta$  decreases, especially for the  $b = 1$  case.

### 3.6.5. The Luminosity in Directed Kinetic Energy of the Jet

The luminosity in directed kinetic energy of the jet ( $L_j$ ), also known as the beam power, can be estimated using

$$L'_j \propto a_L'^2 v_L'^3 n'_a \propto a_L'^2 v_L' P'_L. \quad (28)$$

Thus the ratio  $L'_j/L_j$  can be estimated using the results on  $a'_L$ ,  $P'_L$ , and  $v'_L$ . Figures 16a and 16b are plots of  $L'_j/L_j$  versus  $\theta$

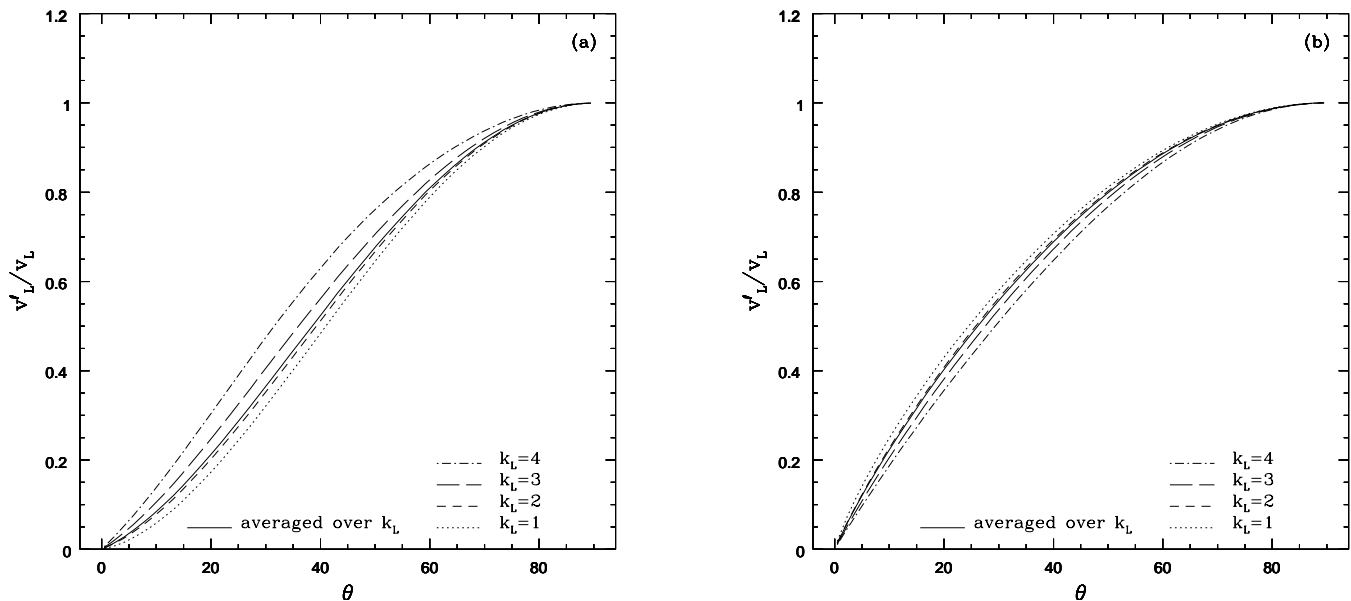


FIG. 14.—Ratio of the observed value of the lobe propagation velocity to the true value as a function of the projection angle for (a)  $b = 1$ , i.e.,  $B = B_{\min}$ , and (b)  $b = 1/4$ , i.e.,  $B = 1/4 B_{\min}$ . The solid curve is the average ratio expected for a sample of sources with the  $k_L$  distribution seen in our sample.

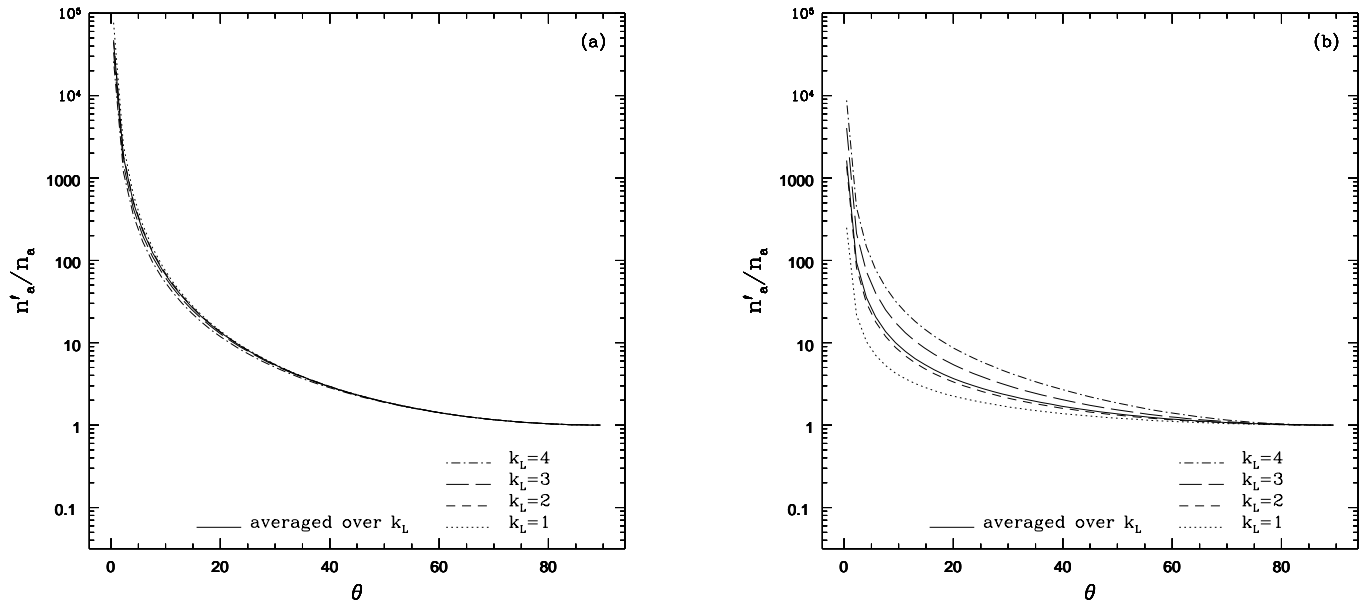


FIG. 15.—Ratio of the observed value of the ambient gas density to the true value as a function of the projection angle for (a)  $b = 1$ , i.e.,  $B = B_{\min}$ , and (b)  $b = 1/4$ , i.e.,  $B = 1/4B_{\min}$ . The solid curve is the average ratio expected for a sample of sources with the  $k_L$  distribution seen in our sample.

for  $b = 1$  and  $b = 1/4$ , respectively. When the projection angle  $\theta \gtrsim 60^\circ$ , the observed value of  $L_j$  is usually within 20% of the true value for both  $b = 1$  and  $b = 1/4$ . For small  $\theta$ , the observed value of  $L_j$  can be quite different from the real value, especially for the  $b = 1$  case.

3.6.6. Characteristic Size of an FR II Source

The study carried out by Daly (1994) showed that FR II sources can be used as powerful cosmological tools when the “characteristic” sizes of the sources, defined as  $D_\star$ , can be estimated. The model gives

$$D_\star \propto v'_L L_j'^{-\beta/3} \propto a'_L{}^{-2\beta/3} v'_L{}^{1-\beta/3} P'_L{}^{-\beta/3}, \quad (29)$$

where  $\beta$  is a parameter in the model that has implications for models of energy extraction from the central engine and

is estimated to be about  $2.0 \pm 0.5$  (Daly 1995; Guerra & Daly 1998). Figures 17a and 17b are plots of  $D'_\star/D_\star$  versus  $\theta$  for  $b = 1$  and  $b = 1/4$ , respectively, assuming  $\beta = 2$ . It appears that  $D_\star$  is not very sensitive to the projection angle. For  $b = 1$ , the observed value of  $D_\star$  is within 20% of the true value with  $\theta > 45^\circ$ . For  $b = 1/4$ , the characteristic size  $D_\star$  appears to be even less sensitive to the projection angle than is the  $b = 1$  case. The observed value of  $D_\star$  is within 20% of the true value when  $\theta > 30^\circ$  and is within 40% of the true value when  $\theta > 10^\circ$ .

3.6.7. The Mach Number of the Lobe Propagation and the Ambient Gas Temperature

WDW97a used the bridge structure of FR II sources to estimate the Mach number of the lobe propagation and the ambient gas temperature. A brief description of the theory is

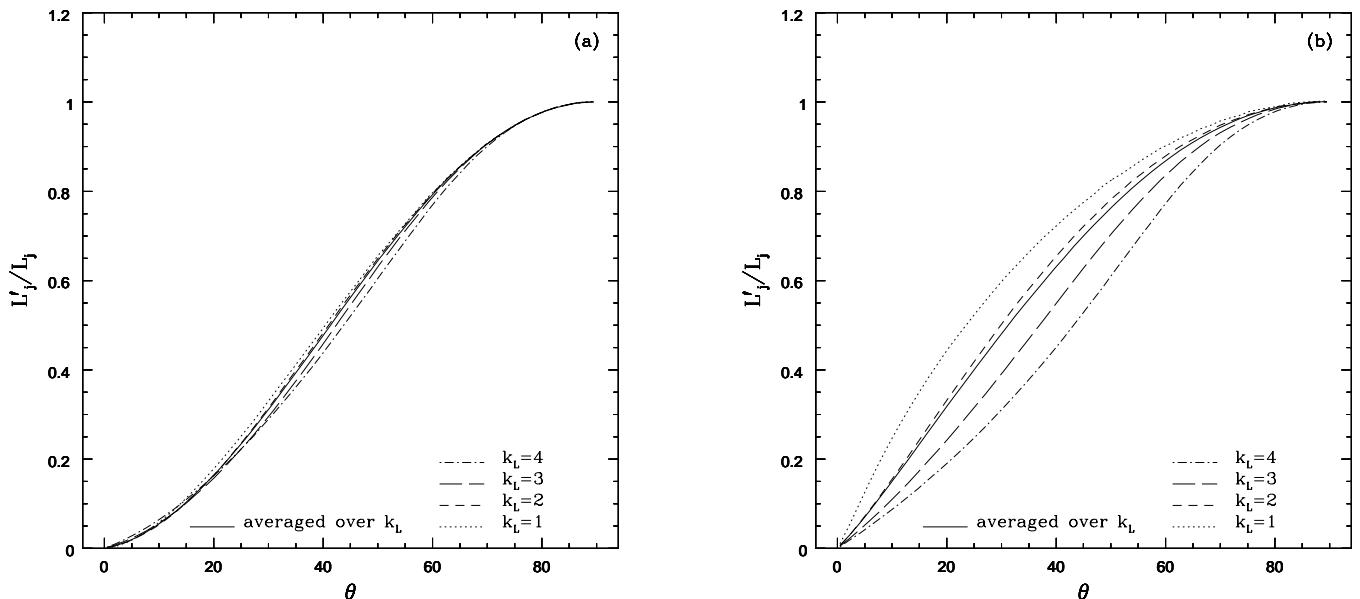


FIG. 16.—Ratio of the observed value of the luminosity in directed kinetic energy of the jet to the true value as a function of the projection angle for (a)  $b = 1$ , i.e.,  $B = B_{\min}$ , and (b)  $b = 1/4$ , i.e.,  $B = 1/4B_{\min}$ . The solid curve is the average ratio expected for a sample of sources with the  $k_L$  distribution seen in our sample.

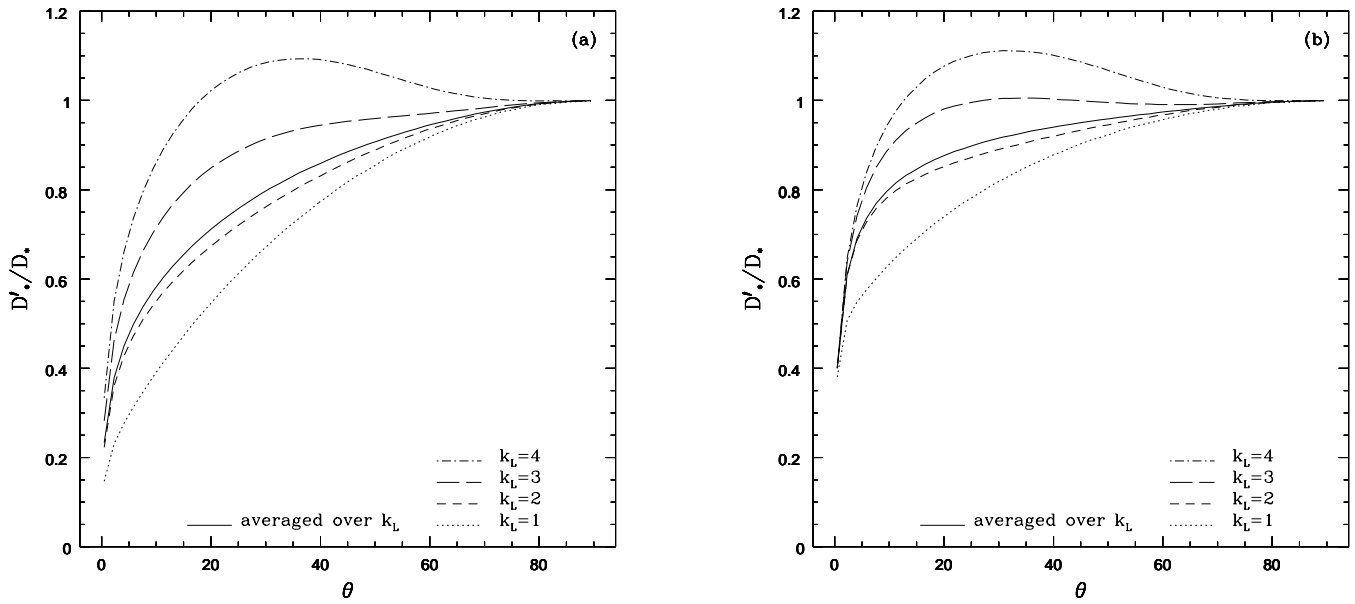


FIG. 17.—Ratio of the observed value of the characteristic size of an FR II source to the true value as a function of the projection angle for (a)  $b = 1$ , i.e.,  $B = B_{\min}$ , and (b)  $b = 1/4$ , i.e.,  $B = 1/4B_{\min}$ . The solid curve is the average ratio expected for a sample of sources with the  $k_L$  distribution seen in our sample.

as follows. When the nonthermal pressure inside the radio bridge of an FR II source is much greater than the ambient gas pressure, the lateral expansion of the bridge is supersonic and has the form  $a(x) \propto x^{1/2}$ . As the bridge expands, the nonthermal pressure inside the bridge decreases and will eventually become comparable to the ambient gas pressure. When this happens, the width of the radio bridge will depart from the  $a(x) \propto x^{1/2}$  expansion law and eventually becomes roughly constant when pressure equilibrium is reached. The lateral expansion velocity at this “break” point is on the order of the sound speed of the surrounding gas ( $c_s$ ), i.e.,

$$\left. \frac{da}{dt} \right|_b \approx c_s. \tag{30}$$

Thus the Mach number of the lobe propagation, defined as  $M = v_L/c_s$ , is

$$M \approx \frac{dx}{dt} \left( \left. \frac{da}{dt} \right|_b \right)^{-1} \approx \left( \left. \frac{da}{dx} \right|_b \right)^{-1}. \tag{31a}$$

Both  $a$  and  $x$  depend on the projection angle. The “break” usually occurs at a fairly large distance from the hotspot, where the ratio  $a'/a$  can be approximated as  $\sin^{-1/2} \theta$  (see § 3.3). Thus the observed value of the Mach number is approximately

$$\begin{aligned} M' &= \left( \left. \frac{da'}{dx'} \right|_b \right)^{-1} \approx \left( \frac{\sin^{-1/2} \theta}{\sin \theta} \left. \frac{da}{dx} \right|_b \right)^{-1} \\ &\approx (\sin \theta)^{3/2} \left( \left. \frac{da}{dx} \right|_b \right)^{-1} \approx M (\sin \theta)^{3/2}. \end{aligned} \tag{31b}$$

Figure 18 shows the ratio  $M'/M$  versus the projection angle  $\theta$ , as given by equation (31b). For  $\theta > 60^\circ$ , the observed value  $M'$  is usually within  $\sim 20\%$  of the real Mach number, whereas for smaller  $\theta$ , the observed  $M'$  can differ from the true  $M$  by a significant amount.

The ambient gas temperature can be estimated by combining  $M$  and the velocity of lobe propagation. The tem-

perature  $T$  is given by

$$T \propto c_s^2 \propto \left( \frac{v_L}{M} \right)^2. \tag{32a}$$

The observed value  $T'$  is simply

$$T' \propto \left( \frac{v'_L}{M'} \right)^2. \tag{32b}$$

It is easy to obtain the ratio  $T'/T$  since both  $v'_L/v_L$  and  $M'/M$  are known (see Figures 14a, 14b, and 18). Figures 19a and 19b are plots of  $T'/T$  versus  $\theta$  for  $b = 1$  and  $b = 1/4$ , respectively. For  $\theta > 60^\circ$ , the observed value of  $T$  is usually

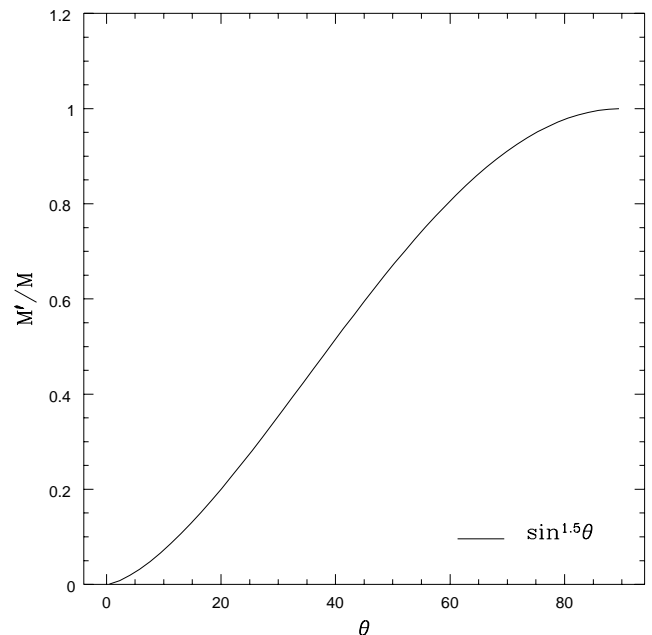


FIG. 18.—Ratio of the observed value of the Mach number of the lobe propagation velocity to the true value as a function of the projection angle.

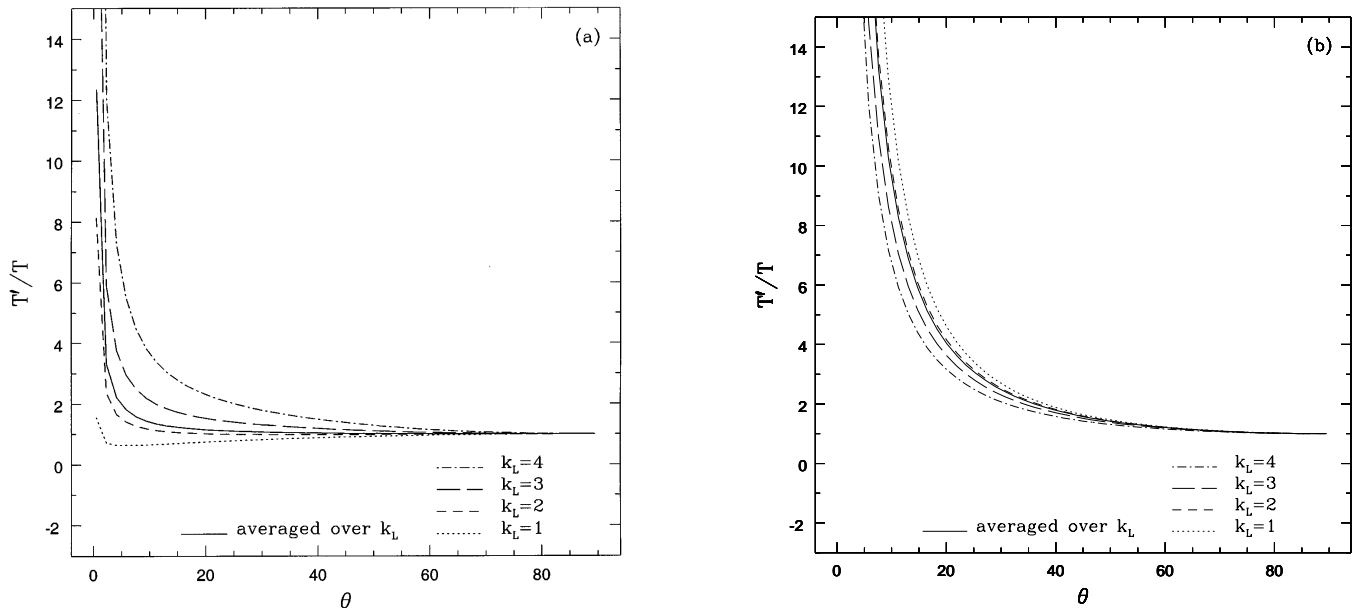


FIG. 19.—Ratio of the observed value of the ambient gas temperature to the true value as a function of the projection angle for (a)  $b = 1$ , i.e.,  $B = B_{\min}$ , and (b)  $b = 1/4$ , i.e.,  $B = 1/4B_{\min}$ . The solid curve is the average ratio expected for a sample of sources with the  $k_L$  distribution seen in our sample.

within 20% of the true value, and for  $\theta > 40^\circ$ , the observed value of  $T$  is usually within a factor of 2 from the true value. This holds for both  $b = 1$  and  $b = 1/4$ . As the projection angle  $\theta$  decreases, the ratio  $T'/T$  increases; the increase is more rapid for the  $b = 1/4$  case.

### 3.7. Summary of Theoretical Results

The discussions presented in this section have shown how empirically determined parameters of an FR II source can be affected by projection effects. Some of the parameters, such as the lobe half-width  $a_L$ , have a rather weak dependence on the projection angle, and their observed values are likely to be close to the true values. As a result, such parameters do not provide a sensitive diagnoses of the projection angle. There are also parameters, such as the ambient gas density  $n_a$ , that are very sensitive to the projection angle. The observed value of these parameters may suffer significant projection effects if the projection angle is small. For large projection angles,  $\theta \geq 60^\circ$  for example, projection effects are unlikely to be important in the estimate of any parameters. The observed value for almost all the parameters studied here is usually within 20% of the true value when  $\theta > 60^\circ$ . The only exception is the ambient gas density  $n_a$ , for which case when  $\theta > 60^\circ$ , the observed value is usually within a factor of about 2 of the true value.

The observed values of projection-sensitive parameters of an FR II source can be used to estimate the projection angle of the source if the intrinsic values of these parameters are known. This is the case for the relation between the decrease in surface brightness and the amount of lateral expansion (see § 3.5). For most parameters, the intrinsic value for a given source is usually not known, so they cannot be used to deduce the projection angle of the individual source. However, if the distribution of the intrinsic value of a parameter is taken to be the same for radio galaxies and for radio-loud quasars, then the apparent difference between the average parameter values for galaxies and quasars can be used to examine whether radio galaxies and radio-loud quasars have similar or different average projection angles.

## 4. EMPIRICAL RESULTS FOR THE SAMPLE

In this section, the theoretical model presented in § 3 is applied to the sample of FR II sources studied here. Various parameters of the radio galaxies and radio quasars in this sample are compared in § 4.1, and in § 4.2 we discuss putting constraints on the projection angles for the sources studied here. A summary of the empirical results is presented in § 4.3.

### 4.1. Differences between Radio Galaxies and Radio-loud Quasars

In the standard orientation-unified model, radio galaxies and radio-loud quasars are drawn from the same parent population but have different orientations with respect to the line of sight. When the radio axis of a radio source lies within a certain critical angle  $\theta_c$  with respect to the line of sight, the source manifests itself as a radio-loud quasar. Otherwise it appears as a radio galaxy. In such a model, the observed differences between radio galaxies and radio-loud quasars are caused solely by their different projection angles, whereas all their underlying physical parameters are the same. Observed values of various parameters of radio galaxies and radio quasars in this sample are compared in the following sections. The ratios of the average values of these parameters of radio-loud quasars to those of radio galaxies are listed in Tables 1 and 2 for  $b = 1/4$  and  $b = 1$ , respectively. Many parameters, such as the linear size of the source, do not depend on the value of  $b$  and are thus listed only in Table 1. Implications of the observed differences, or in some cases of the lack of a difference, between radio-loud quasars and radio galaxies, will be discussed.

The sample studied here is not a complete one and its size is rather small. Thus it is possible the results obtained here might be somewhat different from those obtained for a larger and more complete sample. Instead of performing detailed statistical analyses, we focus on the implications of some general trends seen in the sample. The current sample may suffer from an additional selection effect. As mentioned in § 1, the sample used here combines the large angular size

TABLE 1  
COMPARISON OF QUASARS AND GALAXIES ( $b = 1/4$ )

PARAMETER	AVERAGE VALUE FOR QUASARS/AVERAGE VALUE FOR GALAXIES			PREDICTED RATIO <sup>b</sup>
	$0 < z < 0.9^a$	$0.9 < z < 2$	$0 < z < 2^a$	
$r$ .....	$0.86 \pm 0.21$ (0.78 $\pm$ 0.19)	$0.82 \pm 0.32$	$0.86 \pm 0.17$ (0.83 $\pm$ 0.16)	0.55
$n_a$ .....	$0.47 \pm 0.22$ (0.87 $\pm$ 0.4)	$0.24 \pm 0.1$	$0.5 \pm 0.21$ (0.74 $\pm$ 0.29)	2.05
$v_L$ .....	$0.61 \pm 0.13$ (0.54 $\pm$ 0.11)	$1.71 \pm 0.28$	$1.03 \pm 0.26$ (0.97 $\pm$ 0.25)	0.6
$L_j$ .....	$0.71 \pm 0.29$ (0.68 $\pm$ 0.28)	$1.3 \pm 0.36$	$0.86 \pm 0.33$ (0.81 $\pm$ 0.31)	0.53
$D_*$ .....	$1.11 \pm 0.24$ (1 $\pm$ 0.21)	$1.35 \pm 0.27$	$1.26 \pm 0.2$ (1.21 $\pm$ 0.19)	0.93
$S_L$ .....	$0.22 \pm 0.06$ (0.27 $\pm$ 0.07)	$1.28 \pm 0.48$	$0.71 \pm 0.32$ (0.71 $\pm$ 0.32)	0.65
$P_L$ .....	$0.32 \pm 0.07$ (0.34 $\pm$ 0.08)	$1.32 \pm 0.45$	$0.73 \pm 0.27$ (0.72 $\pm$ 0.27)	0.76
$P_b$ .....	$0.34 \pm 0.08$ (0.39 $\pm$ 0.09)	$2.09 \pm 0.79$	$1.05 \pm 0.42$ (1.07 $\pm$ 0.43)	0.7
$a_L$ .....	$1.9 \pm 0.4$ (1.97 $\pm$ 0.42)	$1.05 \pm 0.27$	$1.52 \pm 0.26$ (1.53 $\pm$ 0.27)	1.09
$k_L$ .....	$1.48 \pm 0.28$ (1.49 $\pm$ 0.3)	$0.96 \pm 0.17$	$1.22 \pm 0.17$ (1.21 $\pm$ 0.17)	1.33

<sup>a</sup> The value in parenthesis is the quasar-to-galaxy ratio when Cygnus A is not included in the galaxy sample.  
<sup>b</sup> The predicted ratio of the average quasar value to the average galaxy value, obtained assuming that  $\langle\theta\rangle_Q = 31^\circ$  and  $\langle\theta\rangle_G = 69^\circ$ , as given by Barthel 1989.

sample of LMS89 with the small angular size sample of LPR92 and thus covers a reasonable range of source sizes. However, since several of the smallest sources from the LPR92 sample are not included in the final sample because of various reasons, it is possible that the final sample is biased against sources of very small sizes, which correspond to sources with very small projection angles in the unified model.

The radio-loud quasars and radio galaxies in this sample have similar radio powers. The ratio of the average quasar radio power at 178 MHz to the average galaxy radio power at 178 MHz is about 1 at both high ( $0.9 < z < 2$ ) and low ( $0 < z < 0.9$ ) redshifts. Thus any differences seen between the radio-loud quasars and the radio galaxies in this sample is unlikely to be caused by differences in their radio power.

4.1.1. Linear Size of the Source

The observed size of a radio source depends on the projection angle as  $r' = r \sin \theta$  (eq. [4]). If radio galaxies and quasars have the same distribution of the true linear size  $r$ , the ratio of the mean observed size of radio-loud quasars to that of radio galaxies is simply  $\langle r' \rangle_Q / \langle r' \rangle_G = \langle \sin \theta \rangle_Q / \langle \sin \theta \rangle_G$ . Barthel (1989) has suggested that  $\langle \theta \rangle_Q = 31^\circ$  and  $\langle \theta \rangle_G = 69^\circ$ , which gives  $\langle r' \rangle_Q / \langle r' \rangle_G = \sin(31^\circ) / \sin(69^\circ) \approx 0.55$ . The linear sizes of the sources studied here are plotted in Figure 20 versus the redshifts of the sources. No apparent difference is seen between radio galaxies and radio-loud quasars. The ratio of the average quasar size to the average galaxy size is about  $0.8 \pm 0.3$ , which is true at both low redshifts ( $0 < z < 0.9$ ) and high redshifts ( $0.9 < z < 2$ ). This ratio is consistent with that obtained by

Barthel (1989). The fact that the ratio of the average quasar size to the average galaxy size does not change with redshift has some interesting implications. Under the orientation-unified model, this suggests that the average projection

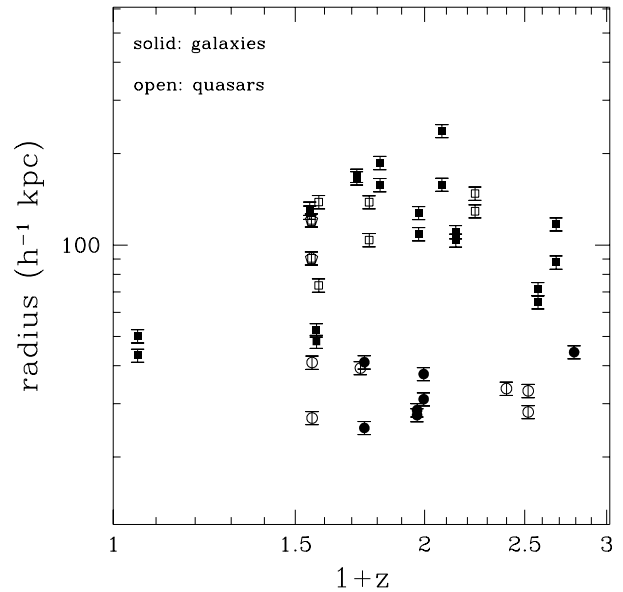


FIG. 20.—Linear size of the FR II sources, represented by the core-hotspot separation, vs. redshift. Circles represent sources from LPR92, and squares represent sources from LMS89. Filled and open signs represent radio galaxies and radio-loud quasars, respectively.

TABLE 2  
COMPARISON OF QUASARS AND GALAXIES ( $b = 1$ )

PARAMETER	AVERAGE VALUE FOR QUASARS/AVERAGE VALUE FOR GALAXIES			PREDICTED RATIO <sup>b</sup>
	$0 < z < 0.9^a$	$0.9 < z < 2$	$0 < z < 2^a$	
$n_a$ .....	$1.14 \pm 0.37$ (1.55 $\pm$ 0.56)	$0.22 \pm 0.08$	$0.89 \pm 0.27$ (1.01 $\pm$ 0.32)	4.25
$v_L$ .....	$0.38 \pm 0.08$ (0.35 $\pm$ 0.07)	$2.04 \pm 0.54$	$1.01 \pm 0.32$ (0.97 $\pm$ 0.31)	0.42
$L_j$ .....	$0.39 \pm 0.14$ (0.39 $\pm$ 0.15)	$1.64 \pm 0.5$	$0.96 \pm 0.39$ (0.92 $\pm$ 0.37)	0.36
$D_*$ .....	$0.97 \pm 0.23$ (0.88 $\pm$ 0.2)	$1.33 \pm 0.22$	$1.16 \pm 0.19$ (1.13 $\pm$ 0.19)	0.83

<sup>a</sup> The value in parenthesis is the quasar-to-galaxy ratio when Cygnus A is not included in the galaxy sample.  
<sup>b</sup> The predicted ratio of the average quasar value to the average galaxy value, obtained assuming that  $\langle\theta\rangle_Q = 31^\circ$  and  $\langle\theta\rangle_G = 69^\circ$ , as given by Barthel 1989.

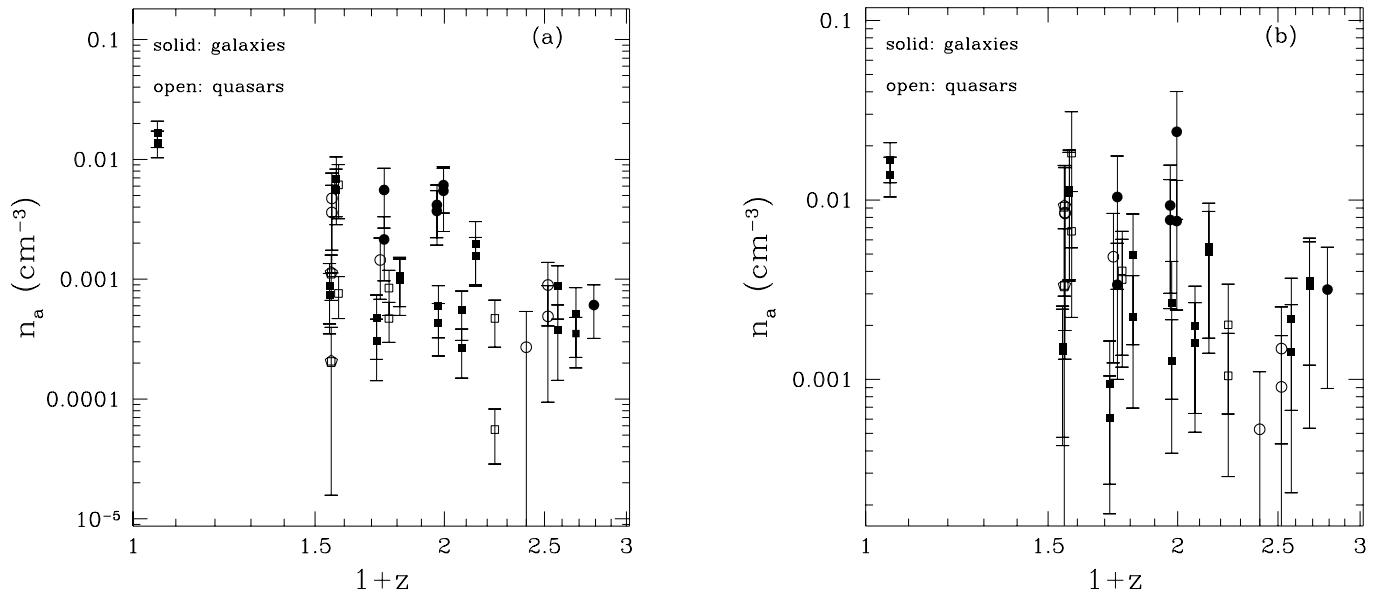


FIG. 21.—Ambient gas density at the vicinity of the radio lobe vs. redshift for (a)  $b = 1/4$ , i.e.,  $B = 1/4B_{\min}$ , and (b)  $b = 1$ , i.e.,  $B = B_{\min}$

angles of radio-loud quasars and radio galaxies are probably not a function of redshift. Thus, the redshift evolution of some parameters, such as the redshift evolution of the ambient gas density and temperature discussed in WDW97a and WDW97b, is probably not caused by an evolution of the projection angle with redshift.

4.1.2. Ambient Gas Density and Other Parameters

The observed value of the ambient gas density is rather sensitive to the projection angle (see § 3.6.4). A difference in the projection angle between radio galaxies and radio-loud quasars will result in different average values of  $n'_a$  for them. Figures 21a and 23b are log-log plots of  $n'_a$  versus  $z$  for  $b = 1/4$  and  $b = 1$ , respectively. For  $b = 1/4$ , the ratio  $\langle n'_a \rangle_Q / \langle n'_a \rangle_G$  at low redshifts is approximately  $0.5 \pm 0.2$  when Cygnus A is included in the galaxy sample and is

about  $0.9 \pm 0.4$  when it is not included (see Table 1). This is to be compared with the predicted value of about 2, obtained assuming that  $\langle \theta \rangle_Q = 31^\circ.0$  and  $\langle \theta \rangle_G = 69^\circ.1$ , as is given by Barthel (1989). The observed value of  $\langle n'_a \rangle_Q / \langle n'_a \rangle_G$  at low redshifts suggests that the average projection angle of the radio-loud quasars in this sample can not be much smaller than, and is probably similar to, that of the radio galaxies. In order to obtain the ratio  $\langle n'_a \rangle_Q / \langle n'_a \rangle_G$  observed at low redshifts,  $\langle \theta \rangle_Q$  has to be greater than  $35^\circ$  at the  $3 \sigma$  level (see Fig. 15b), assuming  $\langle \theta \rangle_G = 69^\circ.1$ , as is given by Barthel (1989). Similar results can be obtained for the  $b = 1$  case (see Table 2 and Fig. 15a). In order to obtain the ratio  $\langle n'_a \rangle_Q / \langle n'_a \rangle_G$  observed at low redshifts,  $\langle \theta \rangle_Q$  has to be greater than  $40^\circ$  at the  $3 \sigma$  level for  $b = 1$ . These constraints on  $\langle \theta \rangle_Q$  will become somewhat larger if  $\langle \theta \rangle_G$  is greater than  $69^\circ.1$ , but the increase will not be signifi-

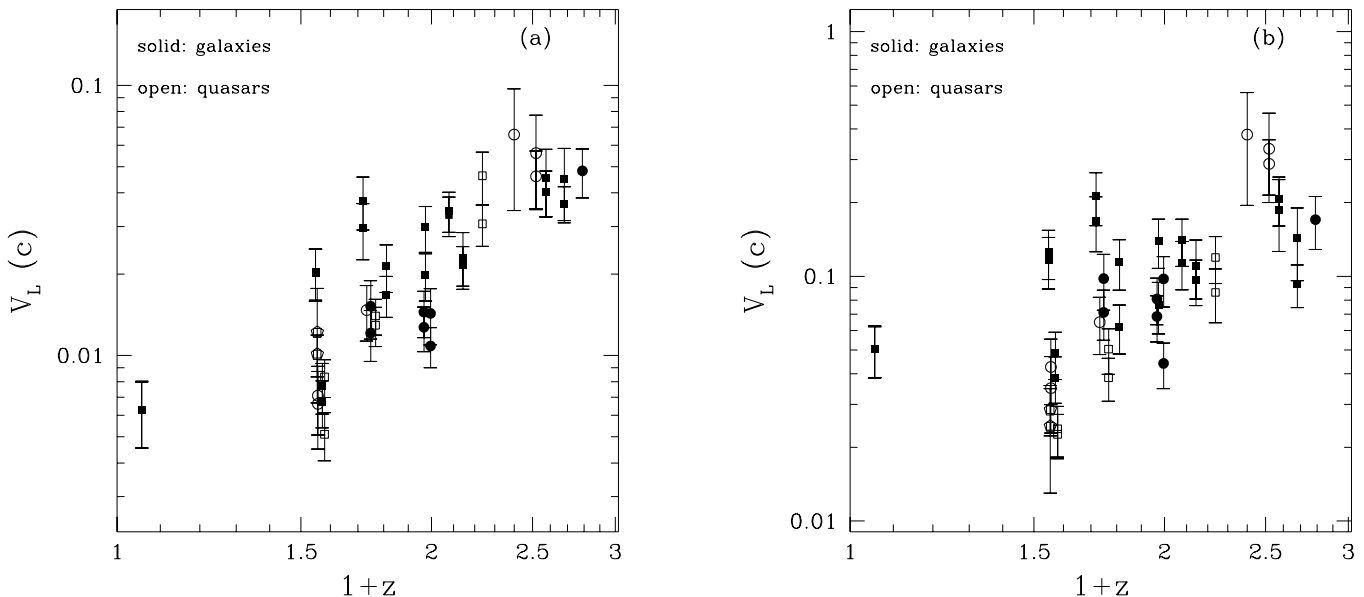


FIG. 22.—Lobe propagation velocity of the FR II source vs. redshift for (a)  $b = 1/4$ , i.e.,  $B = 1/4B_{\min}$ , and (b)  $b = 1$ , i.e.,  $B = B_{\min}$

cant since the value of  $n'_a/n_a$  does not vary much (less than 20%) when  $\theta$  varies from  $69^\circ.1$  to  $90^\circ$ , which holds for both  $b = 1/4$  and  $b = 1$  (see Figs. 15a and 15b). Furthermore, these constraints do not have a strong dependence on the value of  $k_L$ , especially for the  $b = 1$  case. Figure 15 shows that for the  $b = 1$  case, the value of  $n'_a/n_a$  is almost identical for any value of  $k_L$ . Thus, the constraint on  $\langle\theta\rangle_Q$  in this case is independent of  $k_L$ . For  $b = 1/4$ , the spread in  $n'_a/n_a$  for different values of  $k_L$  is somewhat larger than that for  $b = 1$ . However, the  $3\sigma$  lower bound on  $\langle\theta\rangle_Q$  will decrease to only about  $30^\circ$  even if all the sources in the sample have  $k_L = 1$  and will increase if the value of  $k_L$  is greater than about 2. Thus, the constraints on  $\langle\theta\rangle_Q$  obtained above appear to be rather insensitive to  $k_L$ .

The constraints on  $\langle\theta\rangle_Q$  obtained above are somewhat larger than that obtained by Barthel (1989), which may not be surprising since the sample studied here is not complete and is rather small. Note that these constraints on  $\langle\theta\rangle_Q$  are consistent with the observed value of  $\langle r'\rangle_Q/\langle r'\rangle_G$  for this sample and are also consistent with the constraints on the projection angle of the sources in this sample obtained in § 4.2.1, which do not depend on any assumption about the average projection angle of radio galaxies.

At high redshift, the ratio  $\langle n'_a\rangle_Q/\langle n'_a\rangle_G \approx 0.2 \pm 0.1$  for both  $b = 1/4$  and  $b = 1$ . This value is much lower than the predicted value, assuming the average projection angles of radio galaxies and radio-loud quasars given by Barthel (1989), of about 2. This points to rather large projection angles for the high-redshift radio-loud quasars studied here unless there is some real difference between the gaseous environments of radio quasars and of radio galaxies at high redshifts. Note that the high-redshift quasar sample has only five data points. Thus no firm conclusion should be drawn before a larger sample is available.

Figures 22a, 22b, 23a, 23b, 24a, and 24b are plots of the observed values of  $v_L$ ,  $L_j$ , and  $D_\star$  versus  $z$  for  $b = 1/4$  and  $b = 1$ . The ratios of the average observed values of  $v_L$ ,  $L_j$ , and  $D_\star$  for radio-loud quasars to those of radio galaxies are listed in Tables 1 and 2. For these parameters, the observed differences between radio-loud quasars and radio galaxies

are consistent with their being caused by projection effects, given the constraints on  $\langle\theta\rangle_Q$  obtained above, that is,  $\langle\theta\rangle_Q \gtrsim 35^\circ$  to  $40^\circ$  at the  $3\sigma$  level.

Only a fraction of the sources in this sample have measurements of the Mach number of lobe advance  $M$  and the ambient gas temperature  $T$ . This subsample is not large enough to allow meaningful comparison between radio galaxies and radio quasars. A larger sample is needed to compare the values of  $T$  and  $M$  of radio-loud quasars and radio galaxies.

#### 4.1.3. Lobe Surface Brightness, Nonthermal Pressure, and Lobe Width

It appears that projection effects cannot completely explain the differences seen between three parameters of the radio-loud quasars in this sample and those of the radio galaxies. These parameters are the lobe surface brightness ( $S_L$ ), the nonthermal pressure in the radio lobe ( $P_L$ ), and that in the radio bridge ( $P_b$ ). Figures 25, 26, and 27 are log-log plots of the observed values of  $S_L$ ,  $P_L$ , and  $P_b$  versus  $z$ . At low-redshift, radio-loud quasars appear to have lower lobe surface brightnesses and lower lobe and bridge nonthermal pressures than radio galaxies on average. In order to obtain the values of  $\langle S'_L\rangle_Q/\langle S'_L\rangle_G$ ,  $\langle P'_L\rangle_Q/\langle P'_L\rangle_G$ , and  $\langle P'_b\rangle_Q/\langle P'_b\rangle_G$  that are observed at low redshifts, the average projection angle of radio-loud quasars has to be smaller than  $\sim 10^\circ$  (see Table 1 and Figs. 4, 11a, and 11b). This is inconsistent with the constraints on  $\langle\theta\rangle_Q$  obtained in § 4.1.2. Thus, at low redshifts, there appear to be some real differences between the radio-loud quasars and the radio galaxies in this sample, in terms of their lobe surface brightnesses and their lobe and bridge nonthermal pressures, in addition to any possible projection effects.

The observed value of the lobe half-width  $a_L$  does not seem to be sensitive to the projection angle, as was shown in Figure 6, and is likely to be representative of the real value. Figure 28 plots  $a'_L$  versus  $z$  for the sources in this sample. Numerical values of the ratio  $\langle a'_L\rangle_Q/\langle a'_L\rangle_G$  are listed in Table 1. The data seem to suggest that at low redshifts, the radio-loud quasars in this sample have larger lobe widths

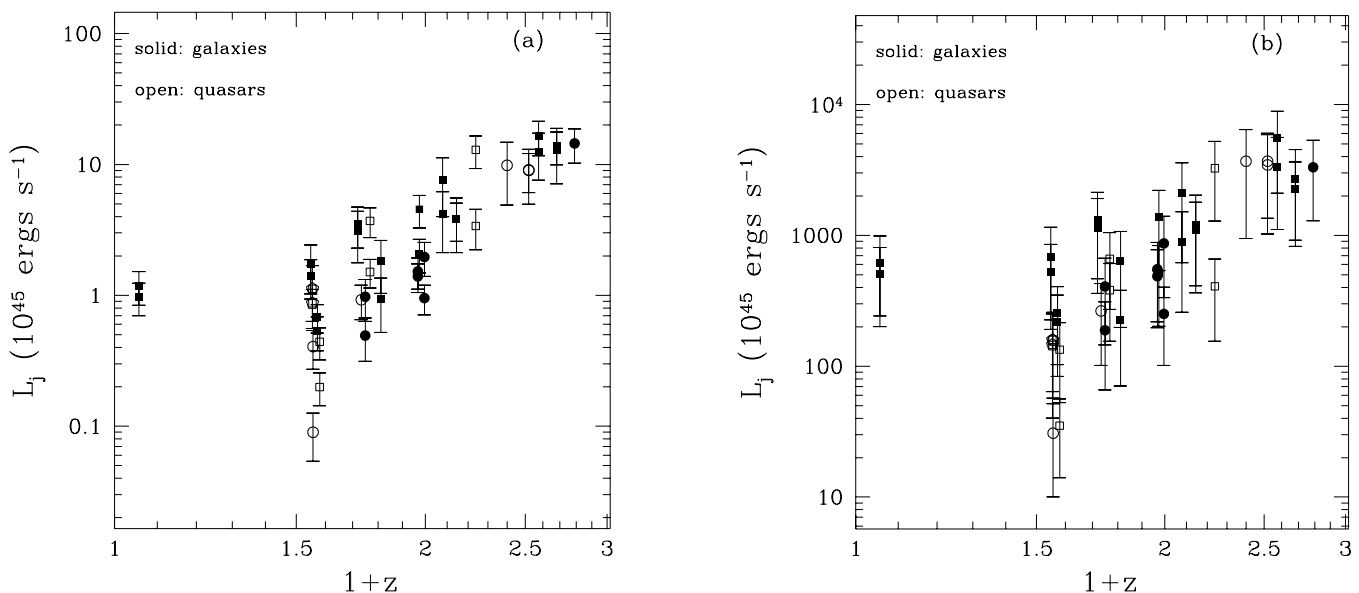


FIG. 23.—Luminosity in directed kinetic energy of the jet of the FR II source vs. redshift for (a)  $b = 1/4$ , i.e.,  $B = 1/4B_{\min}$ , and (b)  $b = 1$ , i.e.,  $B = B_{\min}$

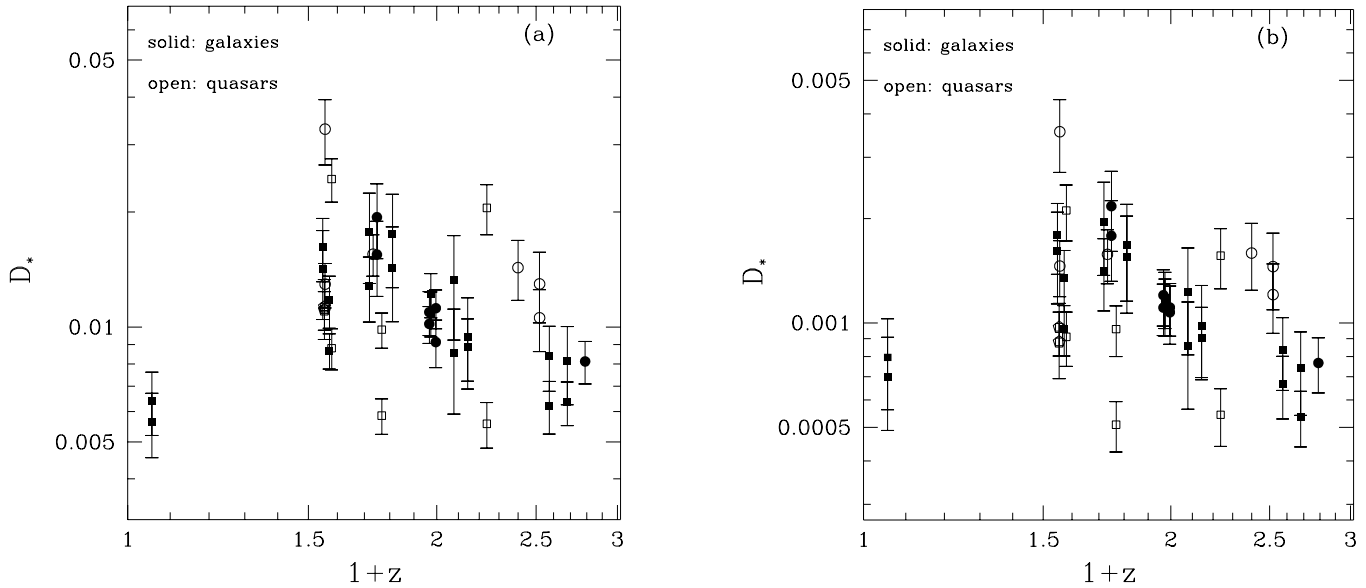


FIG. 24.—Characteristic size of the FR II source vs. redshift for (a)  $b = 1/4$ , i.e.,  $B = 1/4B_{\min}$ , and (b)  $b = 1$ , i.e.,  $B = B_{\min}$

than the radio galaxies on average. This is consistent with the result in LMS89 that radio-loud quasars are typically “fatter” than radio galaxies of similar radio power. For a source with a given radio power, a larger lobe width usually leads to a lower surface brightness. Thus, this offers a possible explanation of the results on the lobe surface brightness and nonthermal pressure: the radio-loud quasars at low redshifts are somewhat “fatter” than the radio galaxies and thus have lower surface brightnesses and nonthermal pressures. Such a picture is also consistent with the fact that the radio-loud quasars at low redshifts appear to have larger  $k_L$  values than do the radio galaxies on average (see Table 1 and Fig. 29).

The above results do not seem to apply at high redshifts, where the radio-loud quasars and radio galaxies seem to

have comparable values of  $S'_L$ ,  $P'_L$ ,  $P'_b$ , and  $a'_L$ . As discussed in § 4.1.2, the high-redshift quasar sample is rather small. A larger sample is needed before a firm conclusion can be drawn.

4.2. Constraints on the Projection Angle

The theoretical results in § 3 provide several potential diagnoses of the projection angle of an FR II source.

One such diagnosis is the shape of the surface brightness profile in a slice perpendicular to the radio axis. At a small projection angle, the observed surface brightness profile shape can differ significantly from that of a homogeneous emissivity model when there is no projection (§ 3.2). Thus, a close study of the surface brightness profile of an FR II source can put useful constraints on its projection angle,

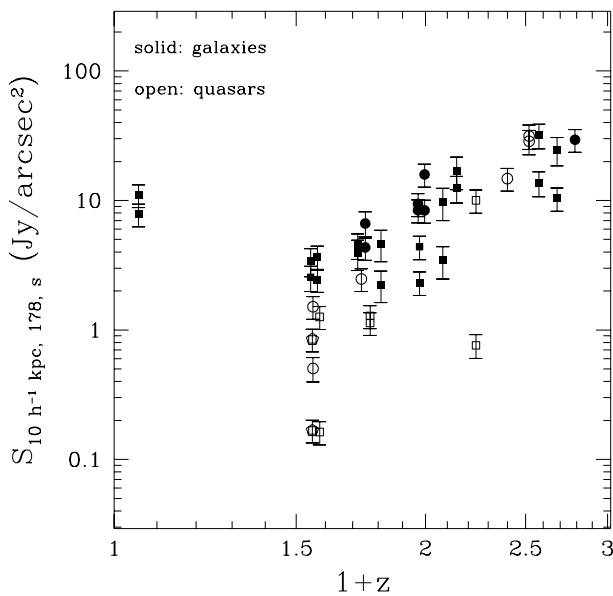


FIG. 25.—Lobe surface brightness of the FR II source, measured at  $10 h^{-1}$  kpc behind the hotspot, vs. redshift.

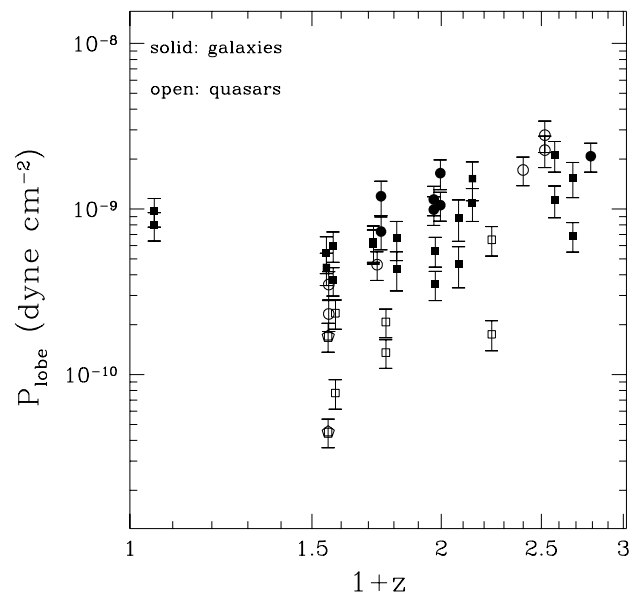


FIG. 26.—Lobe nonthermal pressure of the FR II source, measured at  $10 h^{-1}$  kpc behind the hotspot, vs. redshift for  $b = 1/4$ , i.e.,  $B = 1/4B_{\min}$ .

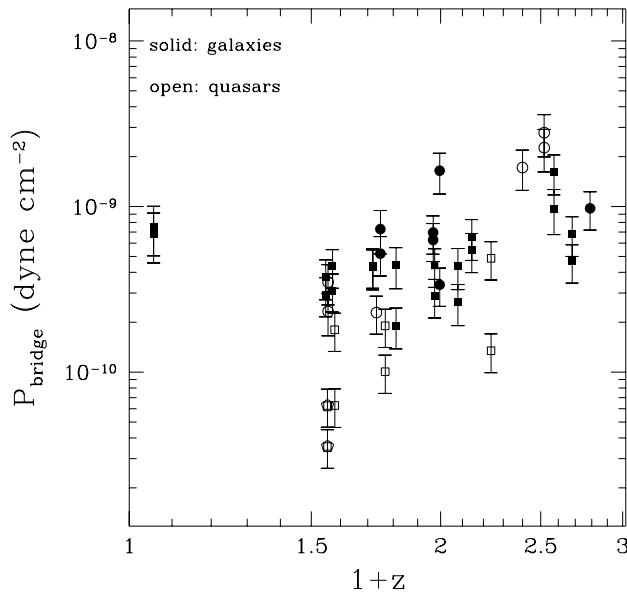


FIG. 27.—Nonthermal pressure in the radio bridge of the FR II source vs. redshift for  $b = 1/4$ , i.e.,  $B = 1/4B_{\min}$ .

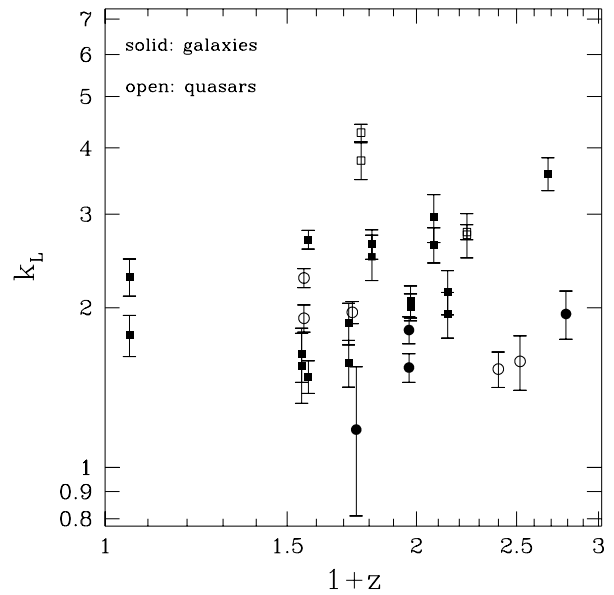


FIG. 29.—Observed value of  $k_L$  vs. redshift for the FR II sources in the sample.

provided that its radio map has high enough resolution. Polarization data can be used to determine whether other factors, such as anisotropic magnetic fields, are important. Unfortunately, the sources studied here usually do not have radio maps with high enough resolution for this method to render useful constraints on their projection angles.

The results from § 3.5 suggest that another good test of whether projection is important is to compare the observed surface brightness with the “predicted” surface brightness under the adiabatic expansion model (eq. [21]). The observed surface brightness traces the “predicted” value if there are no significant projection effects and deviates from the “predicted” value if projection effects are important or if reacceleration of relativistic electrons or backflow are

important. Unfortunately, the uncertainties on the current data for individual sources in this sample are usually too large for this method to yield a useful constraint on the projection angle. The difficulty lies mostly in the fact that if the initial point of lateral expansion is chosen close to the hotspot, the uncertainty on the initial surface brightness will usually be rather large because of possible hotspot contamination, and if the initial point is chosen at a large distance from the hotspot to avoid hotspot contamination, the observed amount of lateral expansion is usually not large enough for projection effects to be significant.

Another way to illustrate this point is as follows. As shown in § 3.5, the best-fit slope ( $n'$ ) of  $\log(S'_0)$  versus  $\log(a')$  is also a measure of projection effects on the observed surface brightness. If projection effects are negligible, the best-fit slope  $n'$  should be close to the predicted slope  $n_{\text{pred}} = 8/3\alpha - 7/3$ . However, as can be seen in Figure 10, the deviation of  $n'$  from the predicted slope caused by projection effect is usually less than 25%, whereas the uncertainty on the observed  $n'$  for a given source in this sample is usually larger than this value. This demonstrates that the current data do not have enough accuracy to detect projection effects by comparing the observed and predicted surface brightnesses.

While the two methods above failed to constrain  $\theta$  with the current data, another method, namely, the study of the departure of the true magnetic field from the minimum-energy magnetic field, seems to work well and yields useful constraint on the projection angles of the sources studied here. This method is described in the following section.

#### 4.2.1. Departure from Minimum-Energy Conditions

WDW97a used three different methods to estimate the ratio of the true magnetic field strength to the minimum-energy magnetic field strength, defined as  $b$ , in the powerful low-redshift FR II source Cygnus A. Each method has a different dependence on the projection angle, so requiring the methods agree can be used to estimate the projection angle. This is done here.

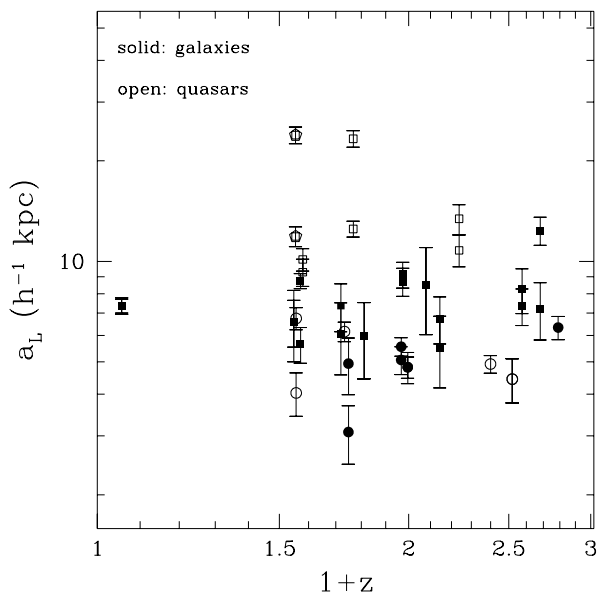


FIG. 28.—Lobe half-width of the FR II source, measured at  $10 h^{-1}$  kpc behind the hotspot, vs. redshift.

The first method to estimate  $b$  is balancing the nonthermal pressure in the radio lobe with the ram pressure. The lobe nonthermal pressure is  $P_L \propto (\frac{4}{3}b^{-1.5} + b^2)B_L^2/24\pi$ , where  $B_L$  is the minimum-energy magnetic field in the radio lobe. For the value of  $b$  of interest here ( $b \sim 0.25$ ), the relation  $b^2 \ll b^{-1.5}$  holds. Hence, the approximation  $P_L \propto \frac{4}{3}b^{-1.5}B_L^2$  holds. The ram pressure is given by  $P_{\text{ram}} = 0.75\rho v_L^2$ , where  $\rho$  is the ambient gas density, estimated using X-ray data. Section 3.6.3 describes how to estimate the lobe propagation velocity  $v_L$ . For Cygnus A, which lies at  $z \sim 0$ ,  $bB_b \gg B_{MB}$ . Thus  $v_L$  can be approximated as  $v_L \propto \Delta D(bB_b)^{3/2}$ , where  $B_b$  is the minimum-energy magnetic field in the radio bridge. Balancing the ram pressure with the lobe nonthermal pressure, it can be shown that the solution of  $b$  has the form  $b^{-9/2} \propto \Delta D^2 B_b^3 B_L^{-2}$ , or,  $b \propto \Delta D^{-4/9} B_b^{-2/3} B_L^{4/9}$ . Not included in this expression of  $b$  are terms that are not affected by projection, such as the break frequency  $\nu_T$  and the ambient gas density  $\rho$  estimated using X-ray data. Since  $P_L \propto B_L^2$  and  $P_b \propto B_b^2$ , this can also be written as  $b \propto \Delta D^{-4/9} P_b^{-1/3} P_L^{2/9}$ . From this it is easy to derive that

$$\frac{b'}{b} \approx \left(\frac{\Delta D'}{\Delta D}\right)^{-4/9} \left(\frac{P'_b}{P_b}\right)^{-1/3} \left(\frac{P'_L}{P_L}\right)^{2/9} \approx (\sin \theta)^{-4/9} \left(\frac{P'_b}{P_b}\right)^{-1/3} \left(\frac{P'_L}{P_L}\right)^{2/9}. \quad (33)$$

The relation  $\Delta D' = \Delta D \sin \theta$  (eq. [4]) is used here. The dependences of  $P'_b/P_b$  and  $P'_L/P_L$  on the projection angle  $\theta$  are all known (see § 3.6.1). Thus it is easy to estimate the ratio  $b'/b$ , which is shown in Figure 30 as the line labeled “ram pressure balance.” The observed value of  $b$ ,  $b'$ , is  $b' = 0.25 \pm 0.02$  (WDW97a).

The second method of estimating  $b$  is to match the ambient gas temperature estimated using the method described in § 3.6.7 with that obtained from X-ray obser-

vation. Equation (32a) gives  $T \propto (v_L/M)^2$ , where  $v_L \propto \Delta D(bB_b)^{3/2}$ . Equating this temperature with the observed X-ray temperature  $T_X$  gives  $b^3 \propto T_X M^2 \Delta D^{-2} B_b^{-3} \propto T_X M^2 \Delta D^{-2} P_b^{-3/2}$ . The X-ray temperature  $T_X$  is independent of projection. Hence, the ratio  $b'/b$  is

$$\frac{b'}{b} \approx \left(\frac{M'}{M}\right)^{2/3} \left(\frac{\Delta D'}{\Delta D}\right)^{-2/3} \left(\frac{P'_b}{P_b}\right)^{-1/2} \approx (\sin \theta)^{1/3} \left(\frac{P'_b}{P_b}\right)^{-1/2}. \quad (34)$$

The relations  $\Delta D' = \Delta D \sin \theta$  (eq. [4]) and  $M' \approx M(\sin \theta)^{3/2}$  (eq. [31b]) are used here. The ratio  $b'/b$  estimated using this method is shown in Figure 30 as the line labeled “temperature match.” The observed value of  $b$ , estimated using this method, is  $b' = 0.32 \pm 0.06$  (WDW97a).

The third method to estimate  $b$  is to equate the nonthermal pressure in the innermost region of the radio bridge, where lateral expansion of the source has ceased, to the thermal pressure of the surrounding gas estimated using X-ray data. The nonthermal pressure can be estimated using equation (23). As mentioned above, for the value of  $b$  of interest here ( $b \sim 0.25$ ), the relation  $b^2 \ll b^{-1.5}$  holds. Thus, the nonthermal pressure can be approximated by  $P \propto \frac{4}{3}b^{-1.5}B_{\text{min}}^2$ . Equating this pressure with the thermal pressure  $P_{\text{th}}$  gives  $b \propto P_{\text{th}} B_{\text{min}}^{4/3}$ . The thermal pressure  $P_{\text{th}}$  is estimated using X-ray data and is not affected by projection of the radio source. As a result, the ratio  $b'/b = (B'_{\text{min}}/B_{\text{min}})^{4/3}$ . Note that the result on  $B'_{\text{min}}/B_{\text{min}}$  in § 3.6.1 is for an expanding bridge model. It can not be used here because, in this region, lateral expansion of the bridge has ceased. When lateral expansion is no longer important, the bridge can be approximated by a cylinder of constant width and constant volume emissivity. For such a cylinder projected at some angle  $\theta$ , the line-of-sight depth scales as  $(\sin \theta)^{-1}$ , so the surface brightness also scales as  $(\sin \theta)^{-1}$ . The shape of the surface brightness profile is not affected by projection, so the width of the source at that point is not affected by projection either. Thus the apparent  $B_{\text{min}}$ , estimated using equation (22), scales as  $(\sin \theta)^{-2/7}$ . This means that

$$\frac{b'}{b} \approx \left(\frac{B'_{\text{min}}}{B_{\text{min}}}\right)^{-4/3} \approx (\sin \theta)^{-8/21} \approx (\sin \theta)^{-0.38}, \quad (35)$$

which is shown in Figure 30 by the line labeled “pressure match.” Balancing pressure in the innermost region of the radio bridge, WDW97a estimated  $b' = 0.21 \pm 0.03$ . However, they also note that this estimate should be treated as a lower limit (see WDW97a for details).

Figure 30 is a plot of  $b'/b$  versus  $\theta$  for these three methods of estimating  $b$ . It can be seen that for the temperature-matching method,  $b'/b \approx 1$  for almost any  $\theta$ . For the other two methods, the dependence of  $b'/b$  on  $\theta$  is not very strong except at small projection angles, where the values of  $b$  estimated using these two methods can be quite different from the true value. All three methods give consistent values of  $b$  for Cygnus A. This suggests that the projection angle of Cygnus A cannot be very small. The three values of  $b$  obtained for Cygnus A can be used to constrain its projection angle. Since the value of  $b$  estimated by balancing thermal and nonthermal pressure at the innermost region of the source is only a lower limit, we will focus on the values of  $b$  estimated using the other two methods. The ratio of the

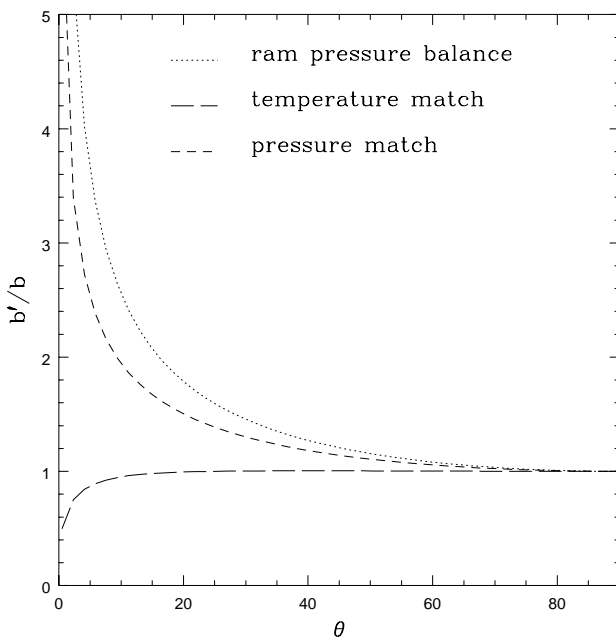


FIG. 30.—Ratios of the observed values of  $b$ , estimated using three different methods (see § 4.2.1), to the true value as a function of the projection angle.

value of  $b$  obtained from the ram pressure balance method to that obtained from the temperature matching method is plotted in Figure 31 versus the projection angle. The observed ratio of the two values and its  $2\sigma$  and  $3\sigma$  boundaries are also shown in the figure. It can be seen that to obtain the observed ratio, the projection angle of Cygnus A has to be greater than  $\sim 40^\circ$  at the  $3\sigma$  level and greater than  $\sim 55^\circ$  at the  $2\sigma$  level. This result is consistent with that obtained by Sorathia et al. (1996), who observed the parsec-scale jet and counterjet in Cygnus A and concluded from their observation that the projection angle of Cygnus A is  $40^\circ \lesssim \theta \lesssim 70^\circ$  for  $h = 1$  and is  $55^\circ \lesssim \theta \lesssim 80^\circ$  for  $h = 0.5$ . Thus it appears that the projection angle of Cygnus A is likely to be rather large, and the observed value of  $b$  is probably not significantly affected by projection effects and is likely to be close to the true value.

WDW97b estimate the maximum possible source to source dispersion of the apparent value of  $b$ ,  $b'$ , in this sample to be about 15% by assuming all of the excess scatter in the composite ambient gas density profile (which caused the reduced  $\chi^2$  of the fit to be greater than 1) comes from a source-to-source dispersion in  $b'$ . Suppose the scatter in  $b'$  comes purely from the scatter in  $\theta$ , which is equivalent to requiring that the dispersion seen in the ambient gas density is caused by different values of  $\theta$ . Then equation (33) can be used to translate the scatter in  $b'$  to the scatter in  $\theta$ . If the projection angle of Cygnus A is greater than  $\sim 40^\circ$ , the projection angles for other sources in the sample have to be greater than  $\sim 30^\circ$  in order for their observed values of  $b$  to differ by no more than 15% from that of Cygnus A, and if the projection angle of Cygnus A is greater than  $\sim 55^\circ$ , the projection angle for other sources in the sample should be greater than  $\sim 40^\circ$ . Note that these constraints on the projection angles of the sources in this sample depend only on the projection angle of Cygnus A, which is constrained by

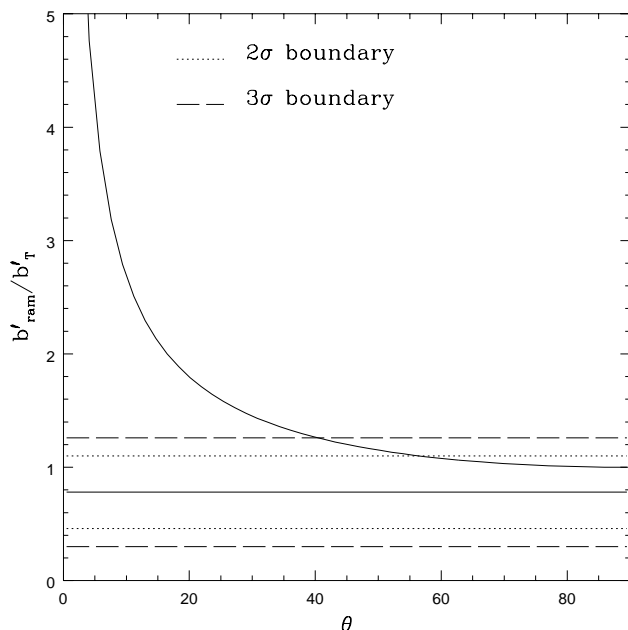


FIG. 31.—Ratio of the observed value of  $b$ , estimated using ram pressure confinement of the radio lobe, to that estimated by matching the ambient gas temperature with the X-ray temperature, as a function of the projection angle. The observed ratio and its  $2\sigma$  and  $3\sigma$  boundaries are also plotted in the figure.

this study and other independent methods. They do not depend on any assumption about the projection angles of radio galaxies and are consistent with the constraints on the average projection angle for radio-loud quasars obtained in § 4.1.2, obtained by assuming that the average projection angle of radio galaxies is about  $70^\circ$ .

#### 4.3. Summary of Empirical Results

Several important results emerge from the empirical studies carried out in this section.

The ratio of the average size of the radio-loud quasars to that of the radio galaxies in this sample has similar value at both high ( $0.9 < z < 2$ ) and low ( $z < 0.9$ ) redshifts, which suggests that the relative projection angles of the radio-loud quasars and the radio galaxies in this sample probably do not evolve strongly with redshift. Thus, the observed redshift evolution of some parameters, such as the ambient gas density and temperature, is probably not caused by an evolution of the relative projection angle.

At low redshifts ( $0 < z < 0.9$ ), comparison between the ambient gas densities of the radio-loud quasars and those of the radio galaxies in this sample suggests that their average projection angles are probably very similar. Assuming that the average projection angle of radio galaxies is about  $70^\circ$  or greater, the average projection angle for the radio-loud quasars in this sample is likely to be greater than about  $35^\circ$ – $40^\circ$  at the  $3\sigma$  level. This is consistent with the results obtained from the study of  $b$  (see § 4.2.1), which do not depend on assumptions about the projection angles of radio galaxies. This value of the average projection angle of radio-loud quasars is somewhat larger than that obtained by Barthel (1989), which may be a result of the fact that this sample is incomplete and rather small and may be biased against sources of very small sizes. Given this constraint on the projection angle of quasars, the current data suggest that, on average, radio galaxies and radio-loud quasars have similar observed values of  $v_L$ ,  $L_j$ , and  $D_{\star}$ , and that the small observed differences between them could be caused by projection effects. However, even after accounting for any possible projection effects, the radio-loud quasars in this sample with  $z < 0.9$  appear to have lower lobe surface brightnesses and lower nonthermal pressures than the radio galaxies on average. A possible explanation is that the radio-loud quasars are “fatter,” that is, they have larger lobe widths, than the radio galaxies on average, as is suggested by LMS89.

Results on the differences between radio-loud quasars and radio galaxies at high redshifts are inconclusive because of the small size of the high-redshift quasar sample. The current data do not suggest substantial differences between the radio-loud quasars and radio galaxies in our sample at that epoch and do not suggest that they have different projection angles. A larger high-redshift sample is needed for further study.

The study of  $b$ , the ratio of the true magnetic field strength to the minimum-energy magnetic field strength, suggests that the projection angle of Cygnus A is likely to be greater than  $\sim 40^\circ$  at the  $3\sigma$  level and to be greater than  $\sim 55^\circ$  at the  $2\sigma$  level. This result is consistent with that given by Sorathia et al. (1996), who suggest that the projection angle of Cygnus A is  $40^\circ \lesssim \theta \lesssim 70^\circ$  for  $h = 1$  and  $55^\circ \lesssim \theta \lesssim 80^\circ$  for  $h = 0.5$ . Furthermore, the observed amount of dispersion in  $b$  for the sources in this sample, including both radio galaxies and radio-loud quasars, sug-

gests that their projection angles are likely to be greater than  $\sim 30^\circ$  if the projection angle of Cygnus A is greater than  $\sim 40^\circ$  and to be greater than  $\sim 40^\circ$  if the projection angle of Cygnus A is greater than  $\sim 55^\circ$ .

### 5. SUMMARY AND DISCUSSION

Theoretical calculations presented here show that different parameters of a classical double radio source can be affected by projection to various degrees. Some parameters, such as the lobe width, are very insensitive to projection, while other parameters, such as the ambient gas density, are very sensitive. However, for sources with projection angles greater than about  $60^\circ$ , the empirically estimated values of all the parameters of interest here are rather close to the true values.

Projection-sensitive parameters, such as the ambient gas density, can be used as diagnoses of the projection angle. The ambient gas densities around the radio-loud quasars in our sample are very similar to those around the radio galaxies on average, contrary to what is expected if the projection angles of the radio-loud quasars in this sample were significantly smaller than those of the radio galaxies, as predicted by the orientation unified model (see, e.g., Barthel 1989). The data suggest that the average projection angle for the low-redshift radio-loud quasars in this sample is likely to be greater than  $35^\circ$ – $40^\circ$  at the  $3\sigma$  level (see § 4.1.2), assuming that the average projection angle of radio galaxies is about  $70^\circ$  or above.

Another way to estimate the projection angle is through the study of  $b$ , the ratio of the true magnetic field strength to that obtained assuming the minimum-energy conditions (§ 4.2.1). The value of  $b$  can be estimated using three independent methods, each method having different dependence on the projection angle. All three methods yield similar values of  $b$  for Cygnus A, which suggests that the projection

angle of Cygnus A is likely to be greater than about  $40^\circ$ – $55^\circ$ . This is consistent with other independent estimates of the projection angle of Cygnus A (Sorathia et al. 1996). The dispersion in  $b$  from source to source suggests that the projection angles of the sources in this sample are likely to be greater than about  $30^\circ$ – $40^\circ$ . This result is independent of any assumptions about the projection angles of radio galaxies and is consistent with the results obtained from the study of ambient gas density.

The constraints on the average projection angle for the radio-loud quasars in this sample are larger than that obtained by Barthel (1989), which may be a result of the fact that the sample studied here is incomplete and rather small and may be biased against sources with very small size.

The constraints obtained above point to rather large projection angles for the sources in this sample. As a result, the key parameters studied here, such as the temperature and density of the ambient gas, probably do not suffer significant projection effects.

While for most of the parameters, the observed differences between radio-loud quasars and radio galaxies are consistent with their being caused by projection, with  $\langle\theta\rangle_Q \gtrsim 35^\circ$  for  $\langle\theta\rangle_G \approx 69^\circ$ , at low redshifts ( $z < 0.9$ ), there appears to be a real difference between the radio-loud quasars and galaxies in this sample in the sense that the radio-loud quasars seem to have lower lobe surface brightness and lower nonthermal pressure than the radio galaxies. This might be a result of their somewhat larger lobe widths than the galaxies (see § 4.1.3).

It is a pleasure to thank Eddie Guerra and Greg Wellman for helpful discussions. This work was supported in part by the US National Science Foundation, the Independent College Fund of New Jersey, and by a grant from W. M. Wheeler, III.

### REFERENCES

- Alexander, P. 1987, *MNRAS*, 255, 27  
 Alexander, P., & Leahy, J. P. 1987, *MNRAS*, 225, 1  
 Antonucci, R. 1993, *ARA&A*, 31, 473  
 Barthel, P. D. 1989, *ApJ*, 336, 606  
 Begelman, M. C., & Cioffi, D. F. 1989, *ApJ*, 345, L21  
 Carilli, C. L., Perley, R. A., Dreher, J. W., & Leahy, J. P. 1991, *ApJ*, 383, 554  
 Daly, R. A. 1990, *ApJ*, 355, 416  
 ———. 1994, *ApJ*, 426, 38  
 ———. 1995, *ApJ*, 454, 580  
 Fanaroff, B. L., & Riley, J. M. 1974, *MNRAS*, 167, 31  
 Fernini, I., Burns, J. O., Bridle, A. H., & Perley, R. A. 1993, *AJ*, 105, 1690  
 Garrington, S. T., Conway, R. G., & Leahy, J. P. 1991, *MNRAS*, 250, 171  
 Gopal-Krishna, Kulkarni, V. K., & Mangalam, A. V. 1994, *MNRAS*, 268, 459  
 Guerra, E. J., & Daly, R. A. 1998, *ApJ*, 493  
 Jaffe, W. J., & Perola, G. C. 1973, *A&AS*, 26, 423  
 Laing, R. A. 1980, *MNRAS*, 193, 439  
 Laing, R. A. 1981, *ApJ*, 248, 87  
 Leahy, J. P., Muxlow, T. W. B., & Stephens, P. W. 1989, *MNRAS*, 239, 401 (LMS89)  
 Liu, R., Pooley, G., & Riley, J. M. 1992, *MNRAS*, 257, 545 (LPR92)  
 Miley, G. K. 1980, *ARA&A*, 18, 165  
 Myers, S. T., & Spangler, S. R. 1985, *ApJ*, 291, 52  
 Sorathia, B., Bartel, N., Beitenholz, M., & Carilli, C. 1996, in *Cygnus A—Study of a Radio Galaxy*, ed. C. L. Carilli & D. E. Harris (Cambridge: Cambridge Univ. Press), 86  
 Wan, L., & Daly, R. A. 1998, *ApJS*, 115, 141  
 Wellman, G. F., & Daly, R. A. 1996a, in *Cygnus A—Study of a Radio Galaxy*, ed. C. L. Carilli & D. E. Harris (Cambridge: Cambridge Univ. Press), 215  
 ———. 1996b, in *Cygnus A—Study of a Radio Galaxy*, ed. C. L. Carilli & D. E. Harris (Cambridge: Cambridge Univ. Press), 246  
 Wellman, G. F., Daly, R. A., & Wan, L. 1997a, *ApJ*, 480, 79 (WDW97a)  
 ———. 1997b, *ApJ*, 480, 96 (WDW97b)